UNIVERSITY OF CALIFORNIA
SANTA CRUZ

REGOLITH RADIATIVE TRANSFER MODEL; APPLICATIONS TO SATURN'S ICY RINGS

A dissertation submitted in partial satisfaction of the
requirements for the degree of

DOCTOR OF PHILOSOPHY

in

PHYSICS

by

Sanaz Vahidinia

June 2010

The Dissertation of Sanaz Vahidinia
is approved:

Professor Frank Bridges, Chair

Professor Douglas N. C. Lin

Doctor Jeffrey N. Cuzzi

Tyrus Miller
Vice Provost and Dean of Graduate Studies

Copyright © by
Sanaz Vahidinia
2010

Table of Contents

List of Figures v

List of Tables ix

Abstract x

Dedication xi

Acknowledgments xii

1 Introduction 1

2 Saturn's F ring grains: aggregates made of crystalline water ice 3
- 2.1 Background 3
- 2.2 Data 5
  - 2.2.1 Filter Band Gaps 11
- 2.3 Modeling 13
  - 2.3.1 Optical constants 15
  - 2.3.2 Christiansen frequency physics 16
  - 2.3.3 Basic radiative transfer for a diffuse ring layer 17
  - 2.3.4 Mie scattering and Diffraction 19
  - 2.3.5 Discrete Dipole Approximation (DDA) 22
  - 2.3.6 Toy Model 25
- 2.4 Conclusion 32
- 2.5 Acknowledgements 33
- 2.6 References 33

3 Regolith radiative transfer model 39
- 3.1 Background 39
- 3.2 Model description 42
  - 3.2.1 Periodic boundary conditions 42
  - 3.2.2 Calculating radiation from the PBC dipole layer 43
  - 3.2.3 Determining the angular distribution of scattered intensity 45

3.3 Tests 53
    3.3.1 Dielectric slab tests 53
    3.3.2 Granular layer 57
3.4 Conclusion 61
    3.4.1 Acknowledgements 61
3.5 References 61

List of Figures

2.1 Illustration of the observing geometry. Top: Cassini ISS image of the planet and ring system with the sun in occultation, blocked by the planet. The bright spot on the planet's limb is light refracted through the planet's upper atmosphere, not the sun itself. The main rings are highlighted by the tiny amount of small, forward-scattering dust grains they contain. The diffuse E and G rings are visible at about 2.8 and 4.0 Saturn radii. The F ring is a very bright band lying just outside the main rings. Bottom: The geometry of the VIMS F ring observation, showing the sun (symbol) behind the planet. Centered on the sun's direction are loci of constant scattering angle Θ (dashed lines); Θ is an angular offset from the sun, as seen from Cassini, and the phase angle $\alpha = \pi - \Theta$. Notice that different ring longitudes θ can have the same phase angle α. Because the spacecraft was quite far from Saturn during this observation, Θ was quite small (1-3° for the observations we discuss here). Our spectra came from calibrated VIMS mosaics in this same geometry; we averaged the F ring I/F longitudinally and integrated it radially in bins such as shown (see section 2). 5

2.2 These panels demonstrate the longitudinal variation of F ring spectra at ultra-high phase angles; the spectra in each phase bin represent different longitudes θ along the F ring having the same phase angle. The spectra in each phase bin are then averaged, since they are all consistent without any gross longitudinal variation in shape. Only one of the four spiky spectral features is real (section 2.1). 7

2.3 Comparison of VIMS spectra at ultra-high phase angle 178.04^o, high phase angle 162.9^o, and low phase angle 19°. The vertical axis is the Equivalent Width, or the radial integral of F ring brightness (section 2). The 1.5 and 2 μm ice bands are clearly present in the lower phase angles, as well as a much wider and deeper 3 μm absorption feature. The ultra-high phase angle (178.04^o) spectrum has been scaled down by a factor of 9, and the 19° spectrum scaled up by a factor of 30, to display on the same plot. In this paper we deal exclusively with normalized spectra and spectral shapes, so normalization constants are irrelevant. 8

2.4 VIMS spectra at ultra high phase angles 177.4-178.5^o and normalized to their values at 2.86μm. Note the increasing peak brightness at higher phase angles. 9

2.5 VIMS spectra of the F ring at different phase angles between 177-178 degrees as shown in figure 2.2, ratioed to a single intermediate phase angle reference spectrum. Only smooth wavelength dependent differences are seen overall, except for noticeable glitches near the three filter band gaps (nominally 1.64μm, 2.98μm, and 3.87μm) and a more subtle glitch near the Christiansen frequency at 2.86μm. 12

2.6 Expanded and doubly normalized plots of spectral regions of possible interest at different phase angles, first normalized as in figure 2.5 above, and again at some wavelength in each *normalized* spectrum. Four spectral regions are shown: the top panel shows the water ice 2μm band region - no glitch at all can be seen. The bottom three panels show regions near the known filter band gaps. The 2.86μm Christiansen feature (2.82-2.90 μm) can be seen to vary slightly with phase angle, but at an even lower level than than the regions near the filter band gaps. In this figure the 3.8μm and 1.6μm filter bands are seen to affect four spectral channels each and the 2.9μm feature is seen to affect five channels. 13

2.7 Expanded and doubly normalized plots of regions of possible interest, as in figure 2.6. In this figure the 2.9μm and 1.6μm filter band gaps may affect only three spectral channels each but the 3.8μm band gap affects four channels. The strange behavior of some of the 2.86μm Christiansen features is related to saturation of some of the nearby spectral channels because of the unexpectedly high I/F (see text). 14

2.8 Optical constants for crystalline ice at 100K (Mastrapa 2008, 2009) (black) and amorphous ice at the same temperature (red) (Hudgins 1993). The crystalline ice real index crosses unity beginning at 2.86μm, whereas the amorphous real index crosses unity at a slightly shorter wavelength. . . 16

2.9 (top) I/F for solid carbon particles (black) and solid crystalline ice particles (red) calculated with a Mie model for the same size distribution (10-30 μm powerlaw) and phase angles ranging from 177.4-178.5^o. The overall spectral shapes for both disparate compositions match very well except for the 2.86μm dip present in the ice spectrum. (bottom) Comparison of VIMS data and Mie-EMT models for crystalline ice particles with different porosities and no internal structure at one phase angle (178°). All the Mie-EMT calculations in this plot have been done with a power law particle size distribution ranging from 10-30 μm, except for the Mie-EMT particle (solid black) which was done for a broader size distribution (5-30 μm), and clearly demonstrates the effect of smaller particles on the fit. Solid ice has the best overall fit, but the band depth is too shallow compared to the data. As the porosity increases, the band depth also increases, but at the expense of the overall fit. 21

2.10 (Top) Mie-EMT calculations show the crystalline ice Christiansen feature, positioned at 2.86μm, matching the observed position of the feature in the VIMS data. However, the amorphous ice feature occurs at a shorter wavelength than observed. (Bottom) VIMS spectra (red) and EMT ice particles with 30$\%$ porosity (black) at various phases ranging from 177.4-178.2 degrees. The size distribution used for fitting the spectra at phases 177.4-178.0 is our standard power law ranging between 10-30 microns (section 2.3.4). Going to phases greater than 178 degrees such as 178.2, requires even a tighter distribution such as 12-30 micron particle radii to properly fit the short wavelength end. Such a small variation of $n(r)$ with longitude is not implausible (see figure 2.2). 23

2.11 Simulated Aggregate (radius 15μm and 30$\%$ porosity) with overlapping monomers of radii r_m. We have explored r_m between 1-3μm here and in the models of thispaper r_m =3μm. The idealization of a single monomer size is diminished because the overlapping monomers form a lumpy aggregate with a range of effective monomer sizes and shapes. 24

2.12 F ring VIMS data (red) modelled with: Mie-EMT crystalline ice particles with a power law size distribution ranging between 10-30 μm in radius and 30% porosity (green), DDA crystalline ice aggregates (black) with the same porosity and three different size distributions. The DDA power law size distributions range between 9.5-33 μm in aggregate radii (solid black), 11.5-33 μm (long black dash), and 12.5-33 μm (short dash). 26

2.13 I/F is the product of phase function P, extinction coefficient Q_{ext}, and albedo ϖ. The left segment is the product of ϖ and P, with Q_{ext} in the middle, and finally the product of all three parameters giving the normalized intensity I/F in the last segment (plots from Mie-EMT runs). The major effect on the depth of the band in the spectrum is from Q_{ext}. 27

2.14 Extinction coefficient Q_{ext} versus phase shift $\rho = 2x(n_r - 1)$, where n_r is the real refractive index, and size parameter $x = 2\pi r/\lambda$. The expression used to plot Q_{ext} here is valid in the ADT regime and is for an absorbing particle with $n_r = 1.02$ and $n_i = 0.08$ (values close to those at the Christiansen frequency at 2.86μ). As we approach the Christiansen frequency, $\rho = 2x(n_r - 1) \ll 1$ where Q_{ext} is monatonically increasing 28

2.15 Multilayer toy model consists of randomly placed, alternating layers of ice and vacuum with complex refractive index m_j and thickness z_j which can vary randomly between 0-6μm. The total length of the multilayer is kept constant at a value representative of the mean diameter of our aggregate size distribution (about 30μm). We generate many realizations of such multilayers, all having the same average density and total thickness. 29

2.16 (left) Transmitted phase difference $\Delta\phi$ (radians) between an ice-air multilayer and single ice layer with 30% porosity and 30μ thickness versus λ (μm). There are three main features in this plot: (1) the phase difference sharp rise and fall about 2.86μm is where the transmitted EM wave accumulates a larger phase change after going through the multilayer interfaces compared to a single layer (see section 3.5); (2) the asymmetric slope of the phase change below and above $\sim 3\mu$m affects the size distribution used in the DDA model (represented by a multilayer) compared to that used in the Mie-EMT model (represented by a single layer) (see section 3.5); and finally (3) another large accumulation of phase change is at 3.1μm where the interfaces of a multilayer play a large role due to the large imaginary index at this wavelength (see right panels for optical constants). However, we don't see this feature in the observed spectrum because the particles are absorbing with a large imaginary index and Q_{ext} never gets small. That is, the energy transmitted thru the particle is negligible and its effects are insensitve to the details of its phase shift, as opposed to the phase-shift-sensitive behavior at the Christiansen frequency where the energy transmitted is significant. 31

3.1 Comparison of Mie-Conel and van De Hulst models (dashed and dotted lines) with laboratory emissivity measurements of granular quartz layer (solid line) for three separate grain size . . . 40

3.2 Schematic of the DDA code operated in the PBC regime, with the TUC shown in the center and image cells arrayed around. I_o indicates the incident flux and I_s indicates the scattered flux. θ is the angle between the incidednt beam and normal axis of the particle layer and ϕ is the azimuthal rotation around the normal of the layer. 43

3.3 Schematic of our approach to determining T in the shadow zone of the TUC. The diffuse reflectivity, will be determined in a similar geometry on the lit side of the TUC. 44
3.4 (top): Comparison of the transmission coefficient, as a function of wavelength, and for two different planes of polarization TE and TM, for a slightly absorbing dielectric slab as calculated on the TUR by our code (red triangles), and as calculated from Fresnel coefficients for the same slab (solid line for TM and dashed for TE). The slab is h =20 dipoles (6 μm) thick with an index of refraction $m = 1.5 + 0.02i$, and the wavelength λ varies between 4.5-9μm (see section 3.2). (bottom): Reflection coefficient comparison for the same slab between DDfields calculation and Fresnels analytical expression. 54
3.5 (top): Reflected intensity in k-space shown on a polar plot with dimensions (θ, ϕ) for three incident radiation angles: θ_o =20°, 40°, and 60° and $\phi_o = 0$ for all cases. The emergent shown as a white circle in the polar plot moves in k-space at the correct emergent angle: $\theta = 20°$, 40° and 60°. 55
3.6 Reflectivity from a dielectric layer for various $|M|kd$ values ranging between 0.4-0.9 compared with Fresnel's analytical solution (top). Bottom panel shows the difference between Fresnel's coefficient and the dielectric slab reflectivity divided by Fresnel's value (percent error). The difference between the two starts taking off at $|M|kd$ = 0.9. 56
3.7 (left): Granular TUC constructed by overlapping monomers with $\%70$ packing fraction. (right) Granular TUC with $\%30$ packing fraction. 57
3.8 Transmitted intensities for various β orientations from a granular layer with $\%70$ filing factor and two mkd criterion (top panels – $|M|kd$=0.5, bottom panels – $|M|kd$=0.8). left panels show abnormal intensities in red and converged intensities in black. We take the average of the converged intensities shown in blue in the right panels. The variation in averaged transmitted intensity is within $\%10$ for the two mkd cases. 58
3.9 Reflected intensities for two realizations (solid and dotted blue, with the average of the two in green) of a granular layer with $\%70$ filling factor and $|M|kd$ = 0.8. The averaged intensity for the same layer with $|M|kd$ = 0.5 is shown in red for comparison. Variations due to granular realizations and larger $|M|kd$ is within an acceptable limit for our initial studies. Its also interesting to note that there is a qualitative difference in the two averaged reflected intensity curves for $|M|kd$ = 0.5 and 0.8. We believe this is due to the change in grain shapes becoming less spherical as the $|M|kd$ criterion is relaxed. 59

3.10 Reflected and transmitted intensity as a function of zenith angle for granular layers of various filling factors. All layers are composed of quartz monomers and incident upon by a 15.5μ beam at 40° zenith angle. The densely packed layer in black is resembling a homogeneous layer with a specularly reflected and directly transmitted peak present at 40°. The less dense layers are more reflective and less transmissive. There is a transition layer at $\%50$ filling factor which has no directly transmitted beam (where interface terms causing phase shift of light as it travels between material and vacuum play an important role in transmission). 60

List of Tables

2.1 Observations used in this study; each is designated by its observation or "cube" number, taken at some observational mid-time. Each cube has spatial extent given by the pixel dimension (12*12, *etc*.), and the integration time (ms) in both the VIS and IR channels. Only the IR channels are used here. 6

Abstract

Regolith Radiative transfer model; applications to Saturn's icy rings

by

Sanaz Vahidinia

In this dissertation I first present work on scattering properties of icy granular aggregates in an application to Saturn's F ring in the mid IR. This work helped us gain a deeper understanding of how mutltiple interfaces present in a granular object affects important spectral features. The granular aggregate study has naturally led us to studying scattering from more complex system of granular particles packed on an extended surface otherwise known as regolith. Due to major shortcomings of current readiative transfer models for regolith surfaces we have developed a regolith radiative transfer model (RRT) based on a first-principles approach to regolith modeling that is essential for near-to-far inf rared observations of grainy surfaces, and is readily configured to answer fundamental questions about popular models with whi ch all remote observations of all airless solar system bodies with granular surfaces are currently interpreted. Our model accounts for wavelength-size regolith particles which are closely packed and can be heterogeneous in composition and arbitrarily shaped.

This is dedicated to Ahmad joon

Acknowledgments

Chapter 1

Introduction

Interpreting remote observations of granular bodies is an important tool in determining the surface composition of all solid bodies in the solar system. The granular surfaces, such as occur on the surfaces of airless solar system bodies are referred to as regoliths. Regolith surfaces are composed of particles of various sizes, often comparable to or smaller than the wavelength in question that scatter light coherently, packed to varying degrees of porosity such that many particles are touching. Popular models by Hapke (*eg.,* 1981, 1999), Shkuratov et al (1999a,b), and others make simplifying assumptions which are valid to varying degrees and which produce results which can differ greatly in their implications about the actual surface material (Poulet et al 2002a, 2003; Shepard and Helfenstein 2007). Modelling such surfaces becomes even more problematic with current models when the regolith grains are *not* large compared to a wavelength (a basic tenet of Hapke and Shkuratov models) and they are *not* well-separated but indeed closely packed, violating the assumptions of “bright cloud” doubling-type models which use Mie scattering as in Spilker et al. (2005).

Modeling a regolith layer generally involves calculating the single scattering albedo of an individual regolith grain, and then using one of the various radiative transfer methods to derive the overall reflection and transmission of a layer composed of many similar grains. Single scattering albedo can be calculated for small particles by using rayleigh scattering and for larger spherical particles, Mie scattering is used. Since Mie scattering is cumbersome to compute in the geometrical optics limit, various ray-optics based approaches are used for particles much larger than the wavelength (Hapke, Shkuratov).

Once the single particle albedo is obtained, then various multiple scattering techniques can be used to derive the layer properties. These popular models such as the N-stream approach DISORT(Hansen and Travis 1974), adding/doubling(Wiscombe 1975(a,b), Plass 1973), analytical treatment using Chandrasekhar's X and Y functions and assuming isotropic scattering (Hapke 1981), two-stream approach using a similarity transform to convert actual forward-scattering particle phase functions and albedo to isotropic scattering (Conel 1969). All these assume independent scatterers with albedos calculated from the methods named above. Some variations on these techniques has been used to capture close packing effects. These include truncating the diffraction lobe of the single particle scattering function (Pollack and Cuzzi 1979), and Lorentz-Lorentz technique for fine powders(ref). These models have been used extensively, however, they fail to capture important features in laboratory and remote spectra of regolith surfaces (Poulet,Shkuratov). Because of the still unsatisfactory agreement with data due to the underlying above, the outlined methods don't rigorously treat the problem. We need another method that is not limited by coherency, shape, and size. Our approach avoids all these frequently inappropriate assumptions by use of the discrete dipole approximation (DDA) which will be described in chapter 3.

To gain more insight into scattering by granular particles, we modeled individual isolated aggregates where close packing of monomers can be studied more simply, and where a unique and previously puzzling application was timely (Cassinni observations of F ring). Part of the close packing effects of monomers in an aggregate is that as electromagnetic radiation transfers though the monomers, it is encountered by layers of interfaces from monomer to air gap to monomer which in turn has a considerable effect on the total scattering from the aggregate. So, we developed a toy model to allow us to understand these interface effects. We found that aggregates are more effective scatterers than uniform particles based on our toy model. Finally we developed the formalism to extend models of this type to regoliths. This involved devising a new approach to modeling intensity in the mean field of a granular slab and transforming it into the angular distribution of scattered intensity. We give our results of this developement in chapter 3.

Chapter 2

Saturn's F ring grains: aggregates made of crystalline water ice

2.1 Background

This chapter describes my study of a single, isolated aggregate with special spectral features which are diagnostic of the aggregate's physical properties. I collaborated with the Visual Infrared Mapping Spectrometer (VIMS onboard Cassini) team to interpret unique, ultra-high phase angle (176-178.5°) observations of Saturn's F ring obtained in 2006. Saturn's stranded F ring lies just outside of the main rings. It consists of a narrow inner core, approximately 50km wide (Murray et al 2008, Bosh et al 1997) surrounded by multiple strands with variable positions and structure (Charnoz et al 2005, Smith et al 1981,1982, Murray and Gordon 1997). Voyager observations led to the discovery of two moons, Prometheus and Pandora, one on either side of the F ring. This configuration led to the belief that these satellites caused and maintained the narrow structure of the F ring. However, a number of arguments have been raised against this idea (Showalter and Burns 1982, Cuzzi and Burns 1988, Barbara and Esposito 2002) and indeed the F ring structure has changed considerably since Voyager (Showalter 2009, Murray et al 2008).

The F ring lies in a very dynamic and perhaps even chaotic environment (Scargle et al 1993, Winter et al 2007) with clumps and strands forming and disappearing on various time scales. The core itself has a 1 km narrow component with an optical depth of 0.1 and centimeter or larger size particles determined by a combination of stellar and radio observations (Lane et al

1982, Tyler et al 1983). Despite its possibly chaotic environment, the core appears to maintain a nearly constant eccentricity and uniform precession rate (Bosh et al 2002, Nicholson et al 1999). This has led to the belief that most of the mass of the F ring is concentrated in this narrow component, which is embedded in a haze of smaller particles spanning 50km. This more diffuse part of the core is mainly composed of $1 - 100\mu$m size particles with a small population of sub-centimeter size particles (Showalter et al 1992). The several outlying strands, extending over perhaps 150km radially, are another variable feature, and have changed since Voyager observations. Cassini has detected more than five strands with a much larger radial span compared to the two or three strands detected by Voyager; the strands appear to have a transient, spiral configuration (Charnoz et al 2005). The core-multistrand structure is itself enveloped in a much broader, 1500km wide region of much lower optical depth.

In this paper we focus on near-infrared spectra of the F ring obtained by VIMS at ultra-high phase angles greater than 177° (figure 2.1), which means the ring falls near the line connecting the spacecraft to the sun, so the observation point is within the forward-diffraction lobe of particles of 10-100 micron size. Because the F ring has low optical depth, the observed brightness will be dominated by single-scattered diffraction. VIMS data are an outstanding tool for this type of observation and analysis because of their broad spectral coverage (0.35-5 μm) and good spectral resolution. The modeling is somewhat simplified because the particle abundance and optical depth are low, so single scattering dominates. In this paper we treat single scattering by several different techniques: Mie theory (assuming spherical particles) and the Discrete Dipole Approximation (DDA) to assess the possibility of irregular aggregates. In our Mie calculations we allow for the effects of porosity using Effective Medium Theory (EMT; Bohren and Huffman 1983, chapter 8)

While the forward scattered light is dominated by diffraction in the ultrahigh phase data, we see that the broad spectral maximum is bifurcated by a narrow dip at 2.86μm, and the familiar 1.5 and 2 μm absorption features are missing (figures 2.2 and 2.3). We can explain both of these spectral surprises in the context of the single scattering diffraction lobe model. The broad peak in the spectra near 2-3μm wavelength implies a peak in the particle size distribution at sizes around $10 - 30\mu$, as we will show (section 3.3). The water ice optical constant has a Christiansen frequency (real index approaches unity) at 2.86μm, and we find that this is what causes the narrow 2.86μm dip. We will show that the precise spectral location of the narrow absorption feature (2.86μm) is a diagnostic of the material (water ice) and even its crystalline state.

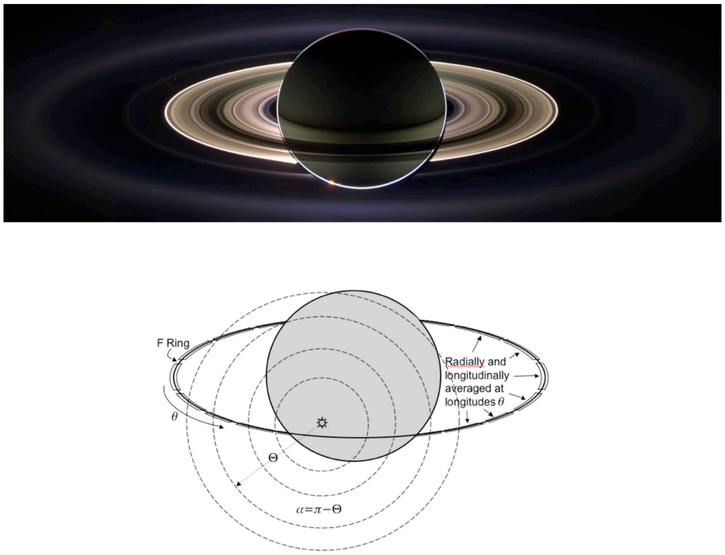

Figure 2.1: Illustration of the observing geometry. Top: Cassini ISS image of the planet and ring system with the sun in occultation, blocked by the planet. The bright spot on the planet's limb is light refracted through the planet's upper atmosphere, not the sun itself. The main rings are highlighted by the tiny amount of small, forward-scattering dust grains they contain. The diffuse E and G rings are visible at about 2.8 and 4.0 Saturn radii. The F ring is a very bright band lying just outside the main rings. Bottom: The geometry of the VIMS F ring observation, showing the sun (symbol) behind the planet. Centered on the sun's direction are loci of constant scattering angle Θ (dashed lines); Θ is an angular offset from the sun, as seen from Cassini, and the phase angle $\alpha = \pi - \Theta$. Notice that different ring longitudes θ can have the same phase angle α. Because the spacecraft was quite far from Saturn during this observation, Θ was quite small (1-3° for the observations we discuss here). Our spectra came from calibrated VIMS mosaics in this same geometry; we averaged the F ring I/F longitudinally and integrated it radially in bins such as shown (see section 2).

2.2 Data

The Visual and Infrared Mapping Spectrometer (VIMS) is described in detail in Brown *et al.* (2004). Briefly, this instrument acquires spectra at 352 wavelengths between 0.35 and 5.2 μm for an array of up to 64×64 spatial pixels to produce a map of the spectral properties in a given scene, known as a cube. Two separate channels measure the visual and infrared components of the spectra. The visual (VIS) channel measures spectra at 96 wavelengths

Cubes	Mid Time	Size	Int (IR, VIS)
Rev 28 HIPHASE001			
V1537007144	2006-258T09:57	64*64	80,5120
V1537008474	2006-258T10:09	64*64	80,5120
V1537009791	2006-258T10:41	64*64	80,5120
V1537023251	2006-258T14:23	12*12	320,3840
V1537023308	2006-258T14:24	12*12	320,3840
Rev 45 HIPHASE001			
V1558904277	2007-146T20:28	64*48	160,10000
V1558904798	2007-146T20:37	64*48	160,10000
V1558905900	2007-146T20:55	64*48	160,10000
V1558906421	2007-146T21:04	64*48	160,10000
V1558907125	2007-146T21:17	64*32	320,20000
Rev 28 HIPHNAC001			
V1537020614	2006-258T13:39	12*12	320,3840
V1537020671	2006-258T13:40	12*12	320,3840
V1537020826	2006-258T13:42	12*12	320,3840
V1537020960	2006-258T13:45	12*12	320,3840
V1537021101	2006-258T13:47	12*12	320,3840
V1537021246	2006-258T13:49	12*12	320,3840
V1537021303	2006-258T13:50	12*12	320,3840
V1537022556	2006-258T14:11	12*12	320,3840
V1537022613	2006-258T14:12	12*12	320,3840
V1537022772	2006-258T14:15	12*12	320,3840
V1537022904	2006-258T14:17	12*12	320,3840
V1537023048	2006-258T14:20	12*12	320,3840
V1537023194	2006-258T14:22	12*12	320,3840

Table 2.1: Observations used in this study; each is designated by its observation or "cube" number, taken at some observational mid-time. Each cube has spatial extent given by the pixel dimension (12*12, *etc.*), and the integration time (ms) in both the VIS and IR channels. Only the IR channels are used here.

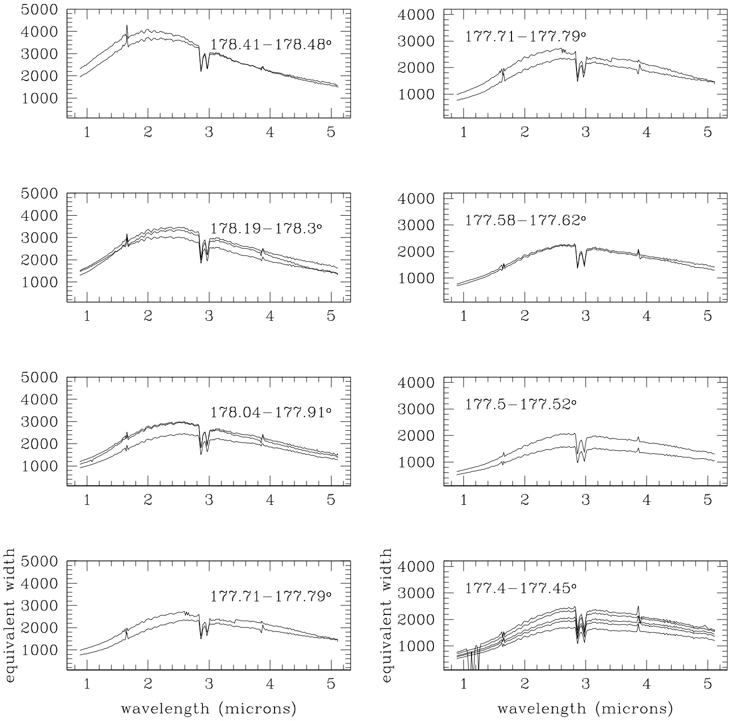

Figure 2.2: These panels demonstrate the longitudinal variation of F ring spectra at ultra-high phase angles; the spectra in each phase bin represent different longitudes θ along the F ring having the same phase angle. The spectra in each phase bin are then averaged, since they are all consistent without any gross longitudinal variation in shape. Only one of the four spiky spectral features is real (section 2.1).

between 0.35 and 1.04 μm, while the infrared (IR) channel measures spectra at 256 points between 0.88 and 5.1 μm with a typical spectral resolution of 0.016 μm. In his paper we only consider the IR channel data, for which the angular resolution was 0.5 milliradians.

The data used in this analysis were obtained during times that Cassini flew through Saturn's shadow. While the disk of the sun was blocked from view, VIMS was able to image the F ring at extremely high phase angles (normally observations are prohibited at phase angles greater than 160 degrees because the remote sensing instruments are not allowed to look too close to the sun). On day 258 of 2006 during orbit 28, Cassini spent a protracted period of time (several hours) in Saturn's shadow and was therefore able to make extensive observations of the ring system. Two sequences of observations obtained during this time will be considered here. The first sequence was named HIPHASE001 and produced a complete mosaic of one ansa of

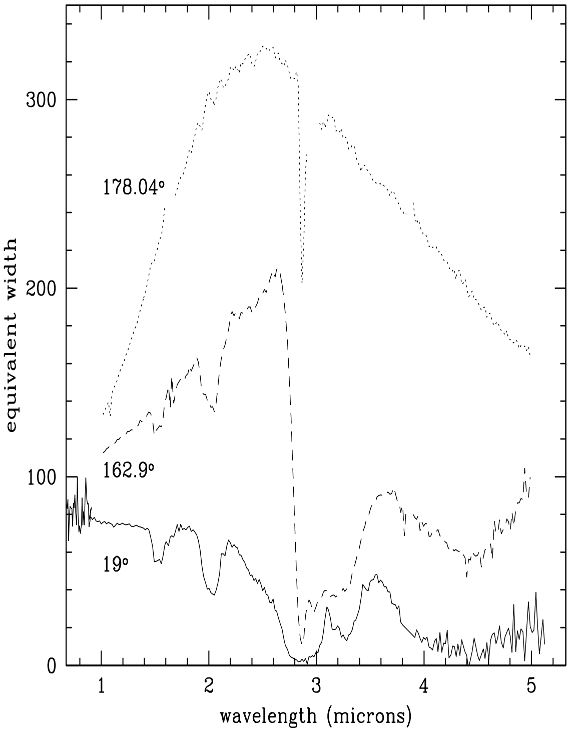

Figure 2.3: Comparison of VIMS spectra at ultra-high phase angle 178.04^o, high phase angle 162.9^o, and low phase angle 19°. The vertical axis is the Equivalent Width, or the radial integral of F ring brightness (section 2). The 1.5 and 2 μm ice bands are clearly present in the lower phase angles, as well as a much wider and deeper 3 μm absorption feature. The ultra-high phase angle (178.04^o) spectrum has been scaled down by a factor of 9, and the 19° spectrum scaled up by a factor of 30, to display on the same plot. In this paper we deal exclusively with normalized spectra and spectral shapes, so normalization constants are irrelevant.

the ring system extending from the planet to outside the core of the E ring. Only the cubes with the shorter integration times are used in this analysis because these were less likely to saturate on the F ring. The second sequence, HIPHNAC, covered both ansae, observing a range of radii and longitudes between the F and D rings. Later, on day 146 of 2007 on orbit 45, Cassini again passed through Saturn's shadow and obtained another series of cubes covering the F ring. Here only five cubes with longer integration times are included in the analysis because the phase angles were not as high as in the orbit 28 data and we wanted to maximize the signal to noise ratio in the F ring.

All the cubes used (listed in Table 1) were calibrated and processed using the standard pipelines to remove dark currents and to convert raw data numbers into the standard measure

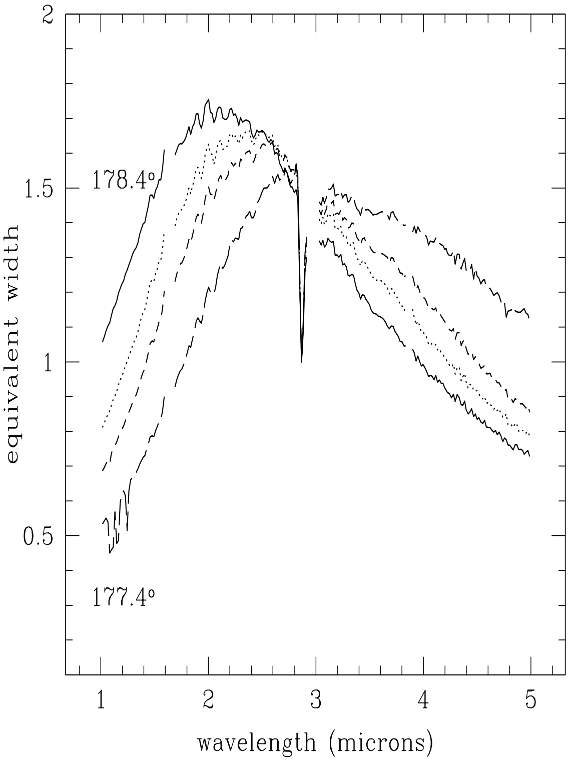

Figure 2.4: VIMS spectra at ultra high phase angles 177.4-178.5° and normalized to their values at 2.86μm. Note the increasing peak brightness at higher phase angles.

of reflectance I/F (the pipeline also outputs specific intensity if you desire it), which is unity for a perfect Lambert surface oriented perpendicular to the incident light (McCord et al. 2004, Cuzzi 1985). The specific calibration curve used with these data was RC17 (technically, RC15 was used to process the cubes, and the final spectra corrected to RC17 using a fixed multiplier at each wavelength). Individual cubes were geometrically navigated based on the available SPICE kernels, and the VIMS pointing was refined based on ring features visible in the individual cubes. This procedure enabled us to determine the observed radius, longitude, phase and emission angle at the ring plane for each pixel in every cube.

The data for each sequence from orbit 28 were then binned onto a grid of radius and longitude values to produce hyper-spectral re-projected mosaics of the rings. The resolutions of these mosaics were 1500 km in radius and 5 degrees in longitude. For each pixel in these re-projected mosaics, we compute the average I/F at each wavelength, along with the mean phase and emission angle. The data from orbit 45 was reduced in a slightly different manner.

Here, each cube covered a relatively small range of longitude (15 degrees) but the phase angle changed significantly between cubes. The data from each cube was therefore averaged over longitude to determine the mean brightness versus wavelength on an evenly spaced set of radii. In this case, the radial bins were 100 km wide. Mean phase angles and emission angles were also computed for each radial bin.

In all cases, the result of this step in the analysis was a series of radial profiles, each giving the brightness as function of wavelength and radius for a restricted range of longitudes and phase angles. Each of these profiles was used to compute a single spectrum of the F ring. Since VIMS was unable to resolve the narrow component of the F ring which dominates the brightness in these observations, as seen for instance in higher-resolution images (figure 2.1), we compute a quantity known as the equivalent width W, which is the integrated brightness over a range of radii: $W = \int (I/F) dr$, this quantity (which has units of length) has the advantage that it is independent of image resolution, unlike the peak brightness. For the rev 28 HIPHASE001 and HIPHNAC data, the brightness was integrated over a radial range between 138,000 km and 142,500 km from Saturn center. For the rev 45 HIPHASE001 data, a mean background I/F level based on the mean I/F between 143,000 and 150,000 km was first removed from each wavelength channel, and then the residual brightness was integrated over the radial range between 137,000 and 143,000 km. The background-subtraction was done in this case because the observations were at a somewhat lower phase angle so the brightness of the F ring relative to the background was significantly lower. These large radial integration ranges include all the F ring core and strand material, plus the 1500km wide extended halo material. They are both wide enough that the I/F contribution near their edges is negligible, so the fact that they are different is of no interest.

The spectra are very sensitive to phase angle and change drastically in shape and magnitude over a few degrees. Since the F ring is clumpy, we examined the spectra for each phase angle at various longitudes to check for variability (see figures 2.2 - 2.4). The spectra of different longitudes were quite similar in shape at the same phase angle, so we averaged the spectra at different longitudes lying in the same phase angle bin.

2.2.1 Filter Band Gaps

The VIMS spectral coverage is interrupted in three narrow wavelength bands, where the change from one order sorting filter to the next causes a low signal. These order sorting filters reduce overlap between different orders of the grating and block thermal radiation from the spectrometer optics so as to reduce noise in the long-wavelength ($> 3\mu$) channels). In our attempts to remove all possible artifacts from our spectra, we identified and rejected a few channels associated with one of these bands which are usually not rejected by the VIMS team; here we document our reasons for doing so.

Under an earlier version of pipeline calibration (RC15), spectral ripples covered the entire spectrum (these have mostly been removed by the RC17 calibration). In order to understand these, we took ratios of spectra at different phase angles; (figure 2.5) shows several of these ratios as functions of wavelength. In the ratio spectra, the worrisome ripples vanished, testifying to their likely instrumental nature and leaving a smooth spectral variation with phase angle which is, however, punctuated by glitches in the regions of the known filter band gaps. Close-up plots of these spectral regions are shown in (figures 2.6 and 2.7, taken from our data sets HIPHASE001 and HIPHNAC respectively. These are doubly normalized spectral plots. After being normalized as above (ratioed to one selected spectrum at some intermediate phase angle), they are next normalized by one of their own (normalized) spectral intensity ratios. The 2.86μm Christiansen frequency (section 2.3.2) shows localized variations, but they are spread over several channels in a systematic way, and vary smoothly with phase angle (the three ratios in (figure 2.7) which sharply decrease to shorter wavelengths connect to saturated points which were designated as zero, so are artifacts). The 2.86μm feature is well away from any filter gaps, and we believe it is real.

The three known filter gap regions all show similar behavior: strong bin-to-bin variations which are not always smoothly or systematically varying with phase angle. These glitches are seen across a well-defined range of wavelengths, but are not generally restricted in their contamination effects to only three wavelength bins (the nominal gap channel and two adjacent channels). In the (slightly) lower phase angle series from HIPHNAC (figure 2.7), one might identify only three corrupted bands in two of the three filter band gaps (1.62, 1.64, 1.65 μm; 2.96, 2.97, 3.00 μm). However, in the HIPHASE001 series (figure 2.6), four or even five wavelengths are corrupted in all cases (1.60, 1.62, 1.64, 1.65), (2.94, 2.96, 2.97, 3.00, 3.01), (3.85, 3.86, 3.88, 3.90), and by comparison it seems to us that the HIPHNAC data (figure 2.7) may be corrupted in the same four channels of the 3.87μm filter gap, as well. For this reason we would prefer not to assign any observational significance to data in any of these broader regions. The VIMS team traditionally rejects at most three channels: the nominal filter gap wavelength and the two adjoining wavelengths. This approach results in F ring spectra apparently containing *two* sharp dips in the 3μm spectral region (figure 2.2); also see Cuzzi et al 2009 and Clark et al 2009). While there is no known reason to expect corruption of the four or five channels where we see what appears to us to be suspicious behavior, the above discussion suggests to us that the longer-wavelength sharp dip seen at 2.95-3.01μm in the VIMS high-phase F ring spectra shown in (figure 2.2) is not real, and we disregard it from our plots and analyses.

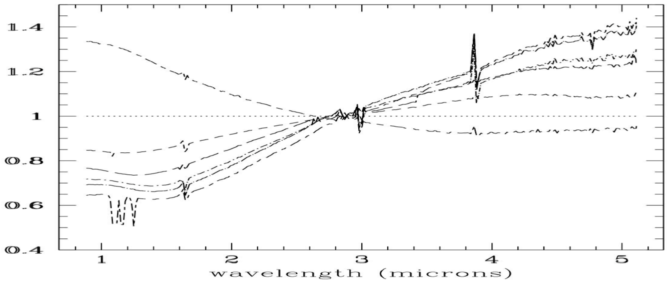

Figure 2.5: VIMS spectra of the F ring at different phase angles between 177-178 degrees as shown in figure 2.2, ratioed to a single intermediate phase angle reference spectrum. Only smooth wavelength dependent differences are seen overall, except for noticeable glitches near the three filter band gaps (nominally 1.64μm, 2.98μm, and 3.87μm) and a more subtle glitch near the Christiansen frequency at 2.86μm.

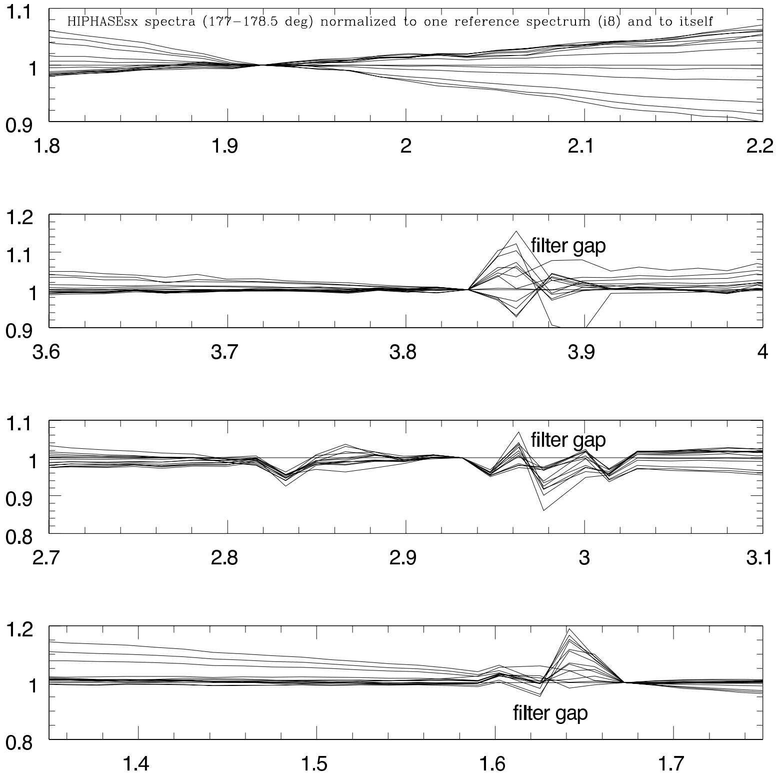

Figure 2.6: Expanded and doubly normalized plots of spectral regions of possible interest at different phase angles, first normalized as in figure 2.5 above, and again at some wavelength in each *normalized* spectrum. Four spectral regions are shown: the top panel shows the water ice 2μm band region - no glitch at all can be seen. The bottom three panels show regions near the known filter band gaps. The 2.86μm Christiansen feature (2.82-2.90 μm) can be seen to vary slightly with phase angle, but at an even lower level than than the regions near the filter band gaps. In this figure the 3.8μm and 1.6μm filter bands are seen to affect four spectral channels each and the 2.9μm feature is seen to affect five channels.

2.3 Modeling

The F ring particles can be modeled as solid spheres, porous spheres, non-spherical solid particles, or non-spherical aggregates. The model consists of a size distribution, which represents the size of a typical ring particle, the composition of the particles as described by their optical constants (sec. 2.3.1 and 2.3.2), and the internal structure of the particle as modeled three different ways: (a) solid, (b) porous but on such a small scale that structure is irrelevant; or (c) porous but composed of monomers with size comparable to the VIMS wavelengths. The first two kinds of particle internal structure can be handled by Mie scattering combined with Effective Medium Theory (EMT; section 2.3.4.1) or by standard irregular particle theories based

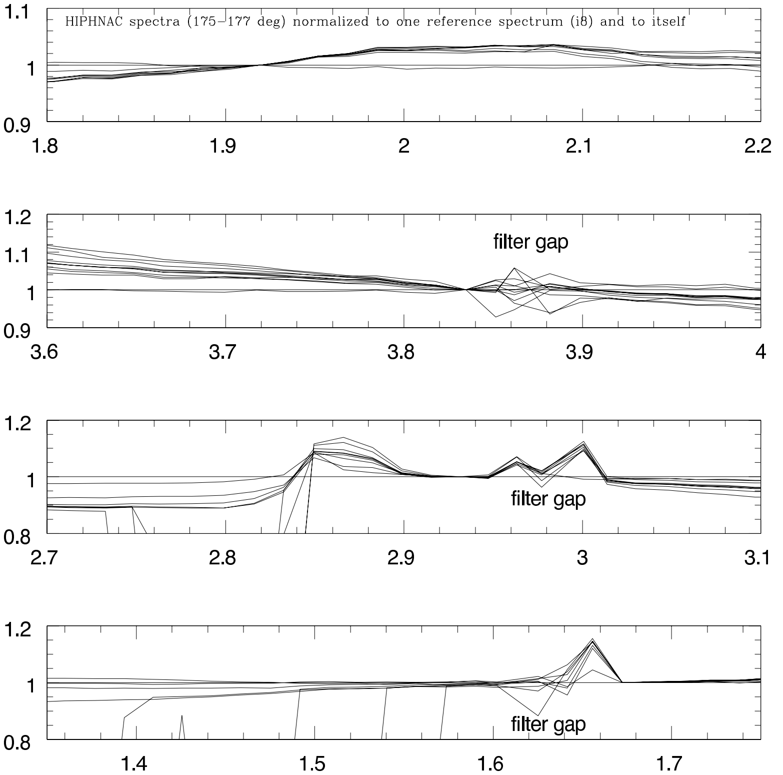

Figure 2.7: Expanded and doubly normalized plots of regions of possible interest, as in figure 2.6. In this figure the 2.9μm and 1.6μm filter band gaps may affect only three spectral channels each but the 3.8μm band gap affects four channels. The strange behavior of some of the 2.86μm Christiansen features is related to saturation of some of the nearby spectral channels because of the unexpectedly high I/F (see text).

on Mie scattering (eg, Pollack and Cuzzi 1980). We did not use this latter approach here; see Hedman et al (2008) for a similar approach using Fraunhofer diffraction to approximate near-forward scattering. The final possibility (c) requires more sophisticated modeling, and for this we used the Discrete Dipole Approximation (DDA). While the DDA is also capable of modeling inclusions of different composition, we do not feel it is justified by the observations at this stage. We can start constraining the particle size distribution, composition, and porosity with the simpler Mie theory and EMT model (section 2.3.4) before moving on to the more complicated discrete dipole model (section 2.3.5).

2.3.1 Optical constants

All scattering calculations use optical constants or refractive indices for the particles of interest; we spent some time selecting the best data set for our purposes. We assume that the F ring particles are composed mostly of water ice with optical constants (real and imaginary refractive indices n_r and n_i respectively) that vary over the temperature range in question. We will further assume the ring particle temperature to be 100K (Esposito et al 1984) and thus will use optical constants valid at this temperature. There are various optical constant data sets that cover water ice at 100K in the near infrared. We considered data for crystalline and amorphous ice from Hudgins et al (1993), Leger et al (1983), Bertie et al (1969, 1977), and Mastrapa et al (2008, 2009). Data from Hudgins et al (1993) and Leger et al (1983) are for amorphous ice (figure 2.8) and data from Bertie et al (1977) are for crystalline ice. Mastrapa (2008, 2009) has the most recent data set for both crystalline and amorphous ice at various temperatures (figure 2.8). This data set is also more finely sampled in wavelength, which results in better modeling of the spectrum. Mastrapa (2008, 2009) obtains the optical constants of ice by measuring the absorption coefficient ($4\pi n_i/\lambda$) through a thin film of ice. These measurements have been done in two separate experiments from 1.1-2.6μm and 2.5-22.0μm. Since we need optical constants from 1-5μm, it is important to have the constants in that range without any discontinuities. For instance, an artificial discontinuity in the ice optical constants near 2.9μm might have corrupted the model spectra of Poulet et al (2003) to some degree (F. Poulet, personal communication 2007). We combined the two data sets by using a Kramers-Kronig analysis on the imaginary index (obtained from the absorption coefficient) of the spectrum to calculate the real refractive index as a function of λ. Since the imaginary index didn't have a smooth crossover between the two overlapping data sets at 2.5μm, we combined the data sets with different smooth bridging functions, and found that they resulted in very similar Kramers-Kronig results. This is because the 3μm band is so strong; the analysis basically tries to capture the largest features in the spectrum, and minor perturbations in lower values of the imaginary index are not contributing factors to the real index. The 3μ band is due to O-H stretching and is composed of two separate components (ν_1 and ν_3), where ν_1 corresponds to the symmetric O-H stretching and ν_3 to the asymmetric O-H stretching (Ockman 1958, Hornig et al 1958).

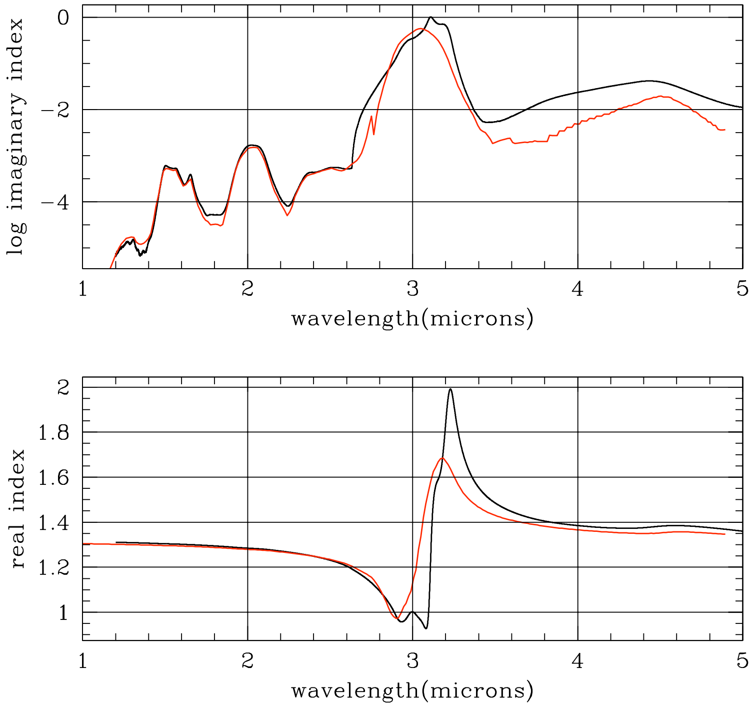

Figure 2.8: Optical constants for crystalline ice at 100K (Mastrapa 2008, 2009) (black) and amorphous ice at the same temperature (red) (Hudgins 1993). The crystalline ice real index crosses unity beginning at 2.86μm, whereas the amorphous real index crosses unity at a slightly shorter wavelength.

2.3.2 Christiansen frequency physics

The water ice 3μm band is interesting because the real part of the refractive index n_r crosses unity multiple times between 2.86 and 3.1μm. The implications of this have been discussed by multiple authors (Conel 1969, Arnott and Hallett 1995, Mustard and Hays 1997); a frequency where $n_r = 1$ is referred to as a Christiansen frequency. When n_r nears 1, and $n_i \ll 1$, the extinction of the incoming EM wave is due primarily to pure absorption within the particle ($\sim 4\pi n_i/\lambda \cdot 2r \ll 1$) since the scattered component (reflection and refraction) is at a minimum and the wave propagates straight through the particle (assuming absorption within the particle remains small). Recalling Huygens' principle, we can see how the intensity of the light scattered by these particles is reduced since the incident wavefront is essentially undisturbed. Thus for a diffraction dominated spectrum at high phase angle (due to wavelength-sized particle contributions), the intensity at some small angular distance from direct forward scattering decreases at the wavelength where $n_r = 1$ (as observed in the F ring spectrum at 2.86μm). There are multiple wavelengths between 2.86-3.1μm where $n_r = 1$, but we only see one dip in the spectrum. This is because at the longer wavelength Christiansen frequency (greater than 2.86 μm) the value of the imaginary index itself is large enough that the particle absorbs radiation traversing it, and by Huygens' principle can contribute to disturbance of the incident wavefront.

Conversely, the Christiansen frequency phenomenon results in an *increase* in the directly transmitted light at this same wavelength, as was observed by Cassini's VIMS during solar occultation observations (Nicholson et al 2007). This effect is complementary to the decrease in near-forward diffraction.

2.3.3 Basic radiative transfer for a diffuse ring layer

This section outlines important radiative transfer concepts used in our Mie-EMT modeling described in section 2.3.4 and DDA modeling described in section 2.3.5. Modeling the F ring as a homogeneous layer of normal optical depth τ, containing N particles with radii r, we calculate the observed I/F as a function of the single particle Mueller scattering matrix $\mathbf{S}$. The Mueller matrix elements relate the Stokes parameters (parameters defining the intensity and state of polarization) of incident and scattered light (this matrix is called F_{ij} in van de Hulst (1957) (from here on referred to as vdH) and Hansen and Travis (1975) (from here on referred to as HT); note below however, they use different conventions for "intensity". For incident unpolarized light, the first Mueller matrix element S_{11} defines the scattered light and will be used in our calculations (see equation 2.1). The derivations of vdH (section 2.1) and HT (section 2) relate what we refer to as the flux density (erg cm^{-2} s^{-1}) scattered by a single particle, as seen at distance R, to the incident flux density which we denote as πF:

$$\frac{F_s}{\pi F} = \frac{\mathbf{S}}{k^2 R^2} \tag{2.1}$$

We reserve the term intensity for flux density per unit solid angle (Chandrasehkar 1960; see also HT section 3). For a scattering system such as a ring, consisting of a volume of N scatterers, having a finite angular extent $d\Omega$ as seen by the observer, the traditional quantity of interest is the intensity I or flux per unit solid angle. Moreover, remote observations normally express the brightness of an extended source as its reflectivity or the ratio of its intensity to the intensity from a perfect Lambert surface, illuminated and viewed at normal incidence, covering the same solid angle, which is $I_L = \pi F/\pi = F$. We thus rewrite equation (1) to address an optically thin layer of scatterers with area A normal to the incident flux and vertically integrated particle surface number density $n(r) = N/A$. Viewed by the observer at an angle θ from the normal to A, where $\mu = cos\theta$, the solid angle subtended by the scatterers is $d\Omega(A, R) = \mu A/R^2$, and the scattered intensity for the particle layer is:

$$I_s(r) = \frac{NF_s}{d\Omega} = \frac{\pi F \ \mathbf{S} \ n(r)}{\mu \ k^2} \tag{2.2}$$

where particle number density $n(r) = n_0 r^{-p}$ for a power law particle size distribution. The Intensity for the layer is then summed over the particle size distribution to get the total scattered intensity (expressed as I/F):

$$\frac{I}{F} = \sum_{r_{min}}^{r_{max}} \frac{\pi S_{11}}{\mu k^2} n_0 r_i^{-p} \Delta r_i, \tag{2.3}$$

We can also relate S_{11} to the standard phase function $P(r) = 4\pi \ S_{11}(r)/k^2 \sigma_{sca}(r)$, where $P(r)$ and $S_{11}(r)$ are functions of scattering angle from the incident direction and particle properties (refractive indices and particle radius r), $k = 2\pi/\lambda$, and scattering cross section $\sigma_{sca}(r)$. The dimensionless efficiency factors for scattering, absorption, and extinction by the particle of size parameter $x = 2\pi r/\lambda$ at wavelength λ are $Q_s(r) \equiv \sigma_{sca}(r)/\pi r^2$, $Q_a(r) \equiv \sigma_a(r)/\pi r^2$, and $Q_{ext}(r) \equiv Q_a(r) + Q_s(r)$. The scattered flux for a single particle can be expressed in terms of its scattering phase function $P(r)$:

$$F_s = \frac{\pi F \ \sigma_{sca}(r) \ P(r)}{4\pi R^2} \tag{2.4}$$

Following equation 2.2, the scattered intensity for a volume of N scatterers can be expressed in terms of $P(r)$:

$$I_s = \frac{NF_s}{d\Omega} = \frac{N\pi F \sigma_{sca}(r) P(r)}{4\pi \mu A} = \frac{FP(r) \ \varpi(r) \ \tau(r)}{4\mu} \tag{2.5}$$

where single particle albedo $\varpi(r) = Q_s(r)/Q_{ext}(r)$, and optical depth is defined as $\tau(r) = n(r)Q_{ext}(r)\pi r^2$. Summing over the particle size distribution we get the total scattered intensity, expressed as I/F:

$$\frac{I}{F} = \varpi P \frac{\tau}{4\mu} = \sum_{r_{min}}^{r_{max}} \frac{\pi S_{11}(r)}{\mu k^2} n_0 r_i^{-p} \Delta r_i, \tag{2.6}$$

where now ϖ, P, and τ are understood to be averaged over the particle size distribution at wavelength λ. The two expressions in equation 2.6 for I/F will be used in our modeling in sections 2.3.4, 2.3.5, and 2.3.6. Also, we are primarily interested in calculating the shape of the spectrum rather than the absolute value of I/F, since the parameter n_o is unknown for the F ring (which means an uncertain optical depth).

2.3.4 Mie scattering and Diffraction

We start with the simplest scenario, in which the ring particles are assumed to be spherical ice particles of uniform but arbitrary density (depending on their porosity), assuming internal structures are much smaller than the wavelength λ, so particles look isotropic and homogeneous to the wave. Mie theory (or even simple diffraction theory; Hedman et al 2008) can be used to calculate scattering from such particles after refractive indices are calculated which are appropriate for the desired porosity (see below in section 3.4.1 for how porosity was treated).

The overall spectral profile at high phase angle is dominated by the diffracted component of the scattered light in the forward direction (Pollack and Cuzzi 1980, Hedman et al 2008). The dominance of diffraction at high phase angle is demonstrated by comparing the spectrum of absorbing carbon particles to that of solid ice particles with the same powerlaw size distribution (figure 2.9). The overall profile of the carbon spectrum must be due to diffraction only, since carbon has negligible contribution to scattering from external reflection and its absorption coefficient is so large that no internal transmission/refraction takes place. Therefore, absorbing particles only diffract light in the near forward direction. The "red" slope at shorter wavelengths (brightness increases with λ) is caused by a deficiency of smaller particles ($r < 10\mu$m) needed to contribute to diffraction at shorter wavelengths at this phase angle, which brings down the intensity at that end. Recall that the width of the diffraction lobe is $\sim \lambda/2r$, thus for some fixed angular offset $180 - \alpha$ from the forward direction, $\lambda/r \sim$ constant. Similarly, at longer wavelengths, the "blue" slope (brightness decreases with λ) is caused by a deficiency of large particles ($r > 30\mu$m). Applying this simple model to solid ice particles with particle radii between $1 - 40\mu$m, we found that the envelope of the F ring spectrum requires a limited width size distribution, which we modeled as a powerlaw (r^{-3}) with radii $r \approx 10 - 30\mu$m (see also Hedman et al 2008). The interesting aspect of this result is that the distribution is somewhat narrow compared to most diffuse ring distributions except the E ring (see Showalter et al 1991 or Throop et al 1998); our approximation by a powerlaw instead of a smooth, unimodal distribution such as Hansen-Hovenier distribution (HT section 2), for instance, may be refined in future studies and is likely not of significance over this narrow size range.

In figure 2.9 the overall profile of the ice and carbon spectra for the same particle size distribution follow the same pattern at various phase angles. This demonstrates that, like the carbon particles, the ice particle spectra are also dominated by diffraction. The carbon particles, of course, do not display a Christiansen feature in this spectral range. Realizing that the scattered light is dominated by diffraction makes it easy to understand the absence of the familiar 1.5 2.0, and 3μm features seen at lower phase angles (figures 2.3 and 2.4) - the amount of light that has entered the ice particle is merely a small perturbation on top of the large diffracted component. This is because the transmitted light, whether absorbed or not, is dispersed by refraction into a far larger solid angle than the diffracted component (HT figure 5).

There is clearly some spectral manifestation of the strong 3μm water ice band, but the shape and even central wavelength of the observed feature are unusual. Its shape is extremely narrow and its central wavelength is at significantly shorter wavelengths than the peak absorption in the ν_3 band (at 3.1μm). It looks nothing like the 3μm absorptions seen at lower phase angles (figure 2.4). This narrow feature is due to the Christiansen effect at 2.86μm, where the real index crosses unity and extinction drops significantly (see sections 2.3.2 and 2.3.6). We find that the two major features of the F ring spectrum - the spectral envelope, which represents only the particle size distribution, and the 2.86μm dip, which is the only manifestation of the optical properties - can be modelled separately. In section 2.3.5 we describe our modeling of the 2.86μm feature.

2.3.4.1 Porous particles analyzed by Effective MediumTheory

Our first models, using solid water ice, failed to give a dip at 2.86μm that was as sharp and deep as the data (see figure 2.9, green curve). Next, we used Effective Medium Theory (EMT) to model porous particles to see if porosity would affect the depth and shape of the 2.86μm band, while leaving the overall spectral envelope unchanged. EMT calculates effective optical constants for a composite/porous particle by averaging over its constituents.

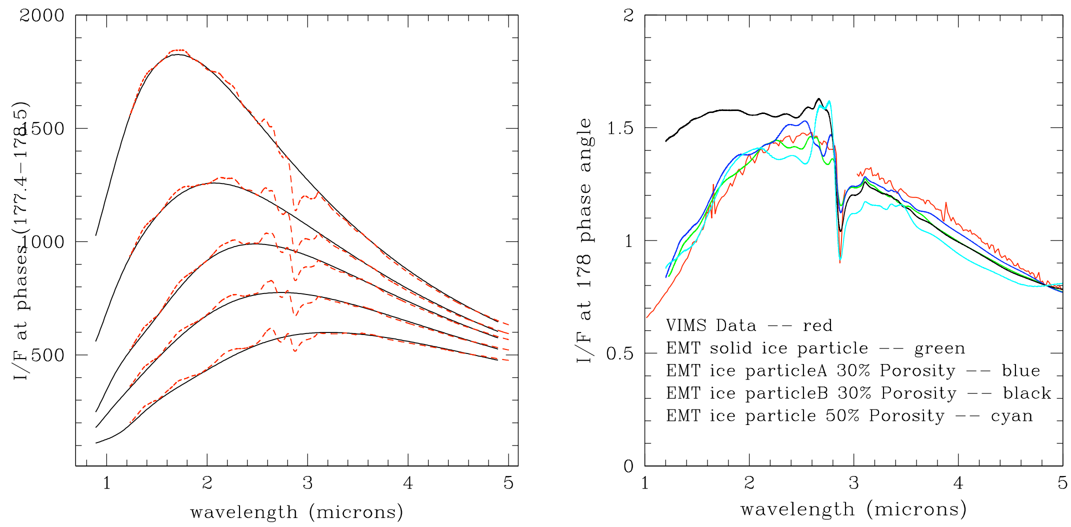

Figure 2.9: (top) I/F for solid carbon particles (black) and solid crystalline ice particles (red) calculated with a Mie model for the same size distribution (10-30 μm powerlaw) and phase angles ranging from 177.4-178.5^o. The overall spectral shapes for both disparate compositions match very well except for the 2.86μm dip present in the ice spectrum. (bottom) Comparison of VIMS data and Mie-EMT models for crystalline ice particles with different porosities and no internal structure at one phase angle (178°). All the Mie-EMT calculations in this plot have been done with a power law particle size distribution ranging from 10-30 μm, except for the Mie-EMT particle (solid black) which was done for a broader size distribution (5-30 μm), and clearly demonstrates the effect of smaller particles on the fit. Solid ice has the best overall fit, but the band depth is too shallow compared to the data. As the porosity increases, the band depth also increases, but at the expense of the overall fit.

There are various flavors of EMT (Bohren and Huffman 1983); our calculations use Maxwell Garnett theory where the average refractive index of a porous particle is calculated by assuming that its solid component contains unresolved vacuum sites or, *vice versa*, small spherical solid particles are distributed in a vacuum “matrix”. The amount of vacuum (porosity) is a free parameter in the calculation and we tested scattering for various porosities. We define the solid volume fraction as f and the porosity as $1 - f$. A simple way to visualize the effects of porosity on scattering is to consider a simple linear expression for the volume-weighted average of the indices which is valid in cases where $|n_r - 1| \ll 1$ and $n_i \ll 1$ with the complex refractive index $m = n_r + in_i$ (van de Hulst 1957, chapter 11), as is true for our spectral range of interest (Cuzzi and Estrada 1998). Since n_i(porous) $= f \cdot n_i$, and n_r(porous) $= 1 + f \cdot (n_r - 1)$, porous particles have n_r closer to unity which causes the extinction efficiency Q_{ext} to be dominated by absorption through the particle. In this regime where $x \gg 1$ and $|m - 1|x \gg 1$, anomalous diffraction theory can be used to get an analytic formula defining Q_a, Q_s, and Q_{ext} (Draine and Allaf-Akbari 2006) which we will use to motivate a toy model of the process (section 3.6). Figure 2.9 shows calculated water ice spectra for different porosities; higher porosity caused the 2.86μm band to get too deep and wide in a relative sense, since it caused the particle albedo and Q_{ext} to increase well away from the 2.86μm dip.

The simple Mie model was useful to constrain the particle size distribution at ultra high phase angles (see figure 2.10) and explain the location and uniqueness of the 2.86μm feature. In figure 2.10, we can see that the position of the 2.86μm dip is better fit by crystalline ice, whereas the amorphous ice spectral dip shifts to a shorter wavelength with respect to the data and crystalline ice. The Mie-EMT approach helped us understand the effects of porosity on the spectrum but it failed to match the 2.86μm band shape qualitatively or quantitatively, so we move on to a different approach (the Discrete Dipole Approximation or DDA) where we assume that the ring particles are aggregates instead of single spherical particles.

2.3.5 Discrete Dipole Approximation (DDA)

The Discrete Dipole Approximation (DDA) is a brute force method, originally introduced by Purcell and Pennypacker (1973); we will utilize the version developed by Draine and Flatau (1994). The DDA is a method of calculating the scattering and absorption of electromagnetic waves by a target object of arbitrary geometry. Target objects are constructed from a regular lattice of individual polarizable dipoles with size smaller than a wavelength (λ) so that the target mimics a homogeneous dielectric material. The dipole spacing is restricted by the criterion $|m|kd \leq 1$, where $m =$ complex refractive index, $k = 2\pi/\lambda$ is the wavenumber, and $d =$ dipole spacing (this forces the optical path length $2\pi md$ to be less than the wavelength λ, and the dipoles act as point scatterers). The polarizability of each dipole can be adjusted to represent the refractive indices of different materials. The polarization state of all dipoles in the system is iterated in response to their individual scattered fields, until a steady state solution is obtained. The overall scattering and absorption cross sections of the array of dipoles are calculated from the final dipole polarization solution. The scattered intensity is calculated from the Mueller Matrix elements S_{ij} obtained from the DDA code (see section 2.3.3, equation 2.3). We define the porosity Φ of our aggregates by using the method of moments developed by Shen et al (2008),

$$\Phi = 1 - f, \tag{2.7}$$

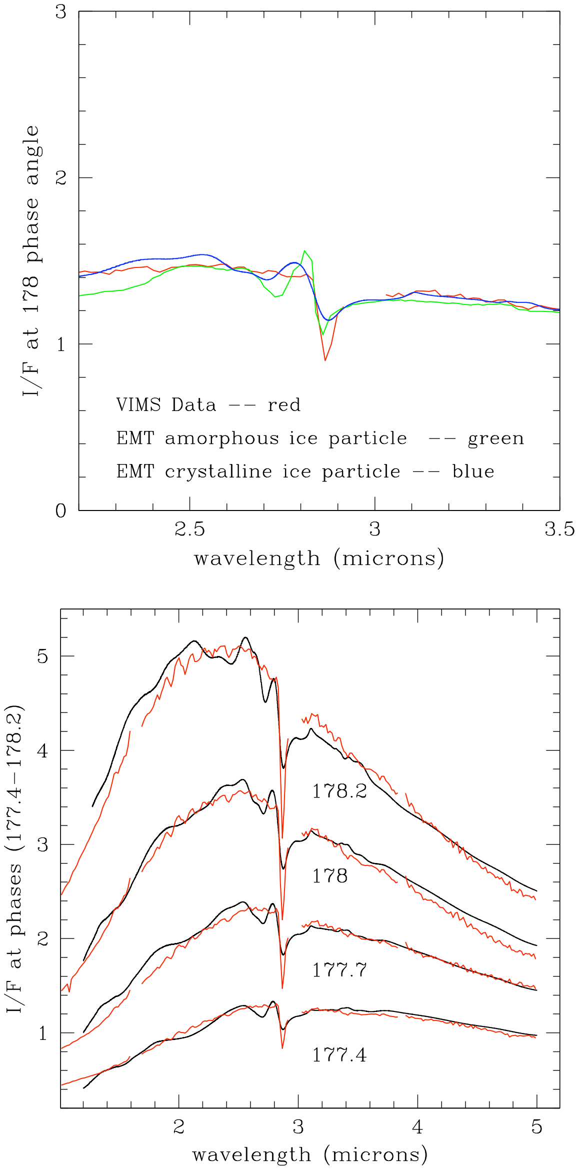

Figure 2.10: (Top) Mie-EMT calculations show the crystalline ice Christiansen feature, positioned at 2.86μm, matching the observed position of the feature in the VIMS data. However, the amorphous ice feature occurs at a shorter wavelength than observed. (Bottom) VIMS spectra (red) and EMT ice particles with 30% porosity (black) at various phases ranging from 177.4-178.2 degrees. The size distribution used for fitting the spectra at phases 177.4-178.0 is our standard power law ranging between 10-30 microns (section 2.3.4). Going to phases greater than 178 degrees such as 178.2, requires even a tighter distribution such as 12-30 micron particle radii to properly fit the short wavelength end. Such a small variation of $n(r)$ with longitude is not implausible (see figure 2.2).

$$\text{filling factor } f = (\alpha_2 + \alpha_3 - \alpha_1)(\alpha_3 + \alpha_1 - \alpha_2)(\alpha_1 + \alpha_2 - \alpha_3)^{-1/2} \tag{2.8}$$

where $\alpha_i = I_i/0.4Ma_{eff}^2$, and I_i is the aggregate's moment of inertia for principal axis i. The radius of a solid, equivalent mass sphere $a_{eff} = r \cdot \Phi^{1/3}$ and the number of dipoles in the aggregate is $N_d = (4\pi/3)(a_{eff}/d)^3$.

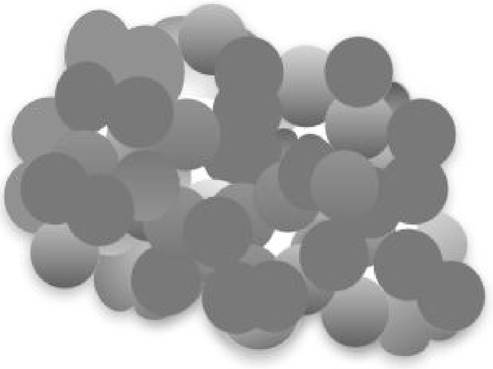

Figure 2.11: Simulated Aggregate (radius 15μm and 30% porosity) with overlapping monomers of radii r_m. We have explored r_m between 1-3μm here and in the models of thispaper r_m =3μm. The idealization of a single monomer size is diminished because the overlapping monomers form a lumpy aggregate with a range of effective monomer sizes and shapes.

From our EMT modeling we find that we need aggregate radii r between 10-30μm with an optical size $x = 2\pi r/\lambda$ ranging from $12 - 33$ at 2.0μm wavelength. The aggregates are composed of individual monomers ranging between 1-3μm in radius r_m (see figure 2.11). The DDA model has recently been optimized by consultants at NASA's HEC Computing facility at Ames Research Center to be able to handle large scatterers such as our aggregates ($2\pi r/\lambda \simeq 100$). The optimized code (http://www.astro.princeton.edu/∼draine/DDSCAT.7.0.html) uses a combination of MPI and OpenMP, where loops within the code are spread out among multiple cpus. The consultants obtained time improvements of about 20 times over the unparallelized version (DDSCAT6.0), and we run on a fast system using typically 64 cpus.

The aggregates are simulated by first picking the desired aggregate envelope size from the size distribution constrained by the Mie-EMT model, a porosity, and a monomer radius r_m. The monomer centers are selected randomly within a sphere of radius r_{agg} and assigned radii; the ensuing spherical monomers can overlap so, even though r_m is constant for an aggregate, a degree of lumpiness or irregularity is present (figure 2.11). We fill the aggregate with such monomers until the desired porosity Φ is reached. We explored r_m =1-3μm, which produced little difference, and settled on r_m =3μm. The aggregate is then populated with dipoles which reside on a regular grid in (x, y, z) and fill the volume stipulated by the placement of the monomers. The dipole size needed to satisfy the DDA criteria $mkd = 1$ is calculated. We have not done convergence tests but since we are primarily interested in integrated quanitites such as Q_e, rather than details of, for instance, the polarization or phase function, $mkd = 1$ will be satisfactory for our calculations. The scattering calculations are averaged first over a series of 32 orientations for a given realization of an aggregate, then over alternate realizations of the monomers within the same size aggregate, and finally over a size distribution of similarly averaged aggregates.

Figure 2.12 shows the results from DDA aggregates using three different size distributions and 30$\%$ porosity, compared to a Mie-EMT calculation of similiar porosity and to VIMS data at 178° phase angle. The DDA size distribution is coarsely binned using 10-12 aggregate sizes. The noisy oscillations at wavelengths shorter than 2.86 μm are due to coarse size sampling and diminish as more size bins are used. The Christiansen feature band depth modeled with this approach is a much closer match to the VIMS data. However, the overall spectral fit is degraded at short wavelengths when the same size distribution as that of Mie-EMT modeling is used. Adjusting the size distribution to contain fewer small particles brings down the short wavelength end of the spectrum (see figure 2.12) but simultaneously widens the 2.86μm band somewhat. Further refinements of the model involving size binning, porosity, monomer sizes or size distributions, *etc.* might be profitably pursued, but the DDA models are quite lengthy to run and we feel at this point that the aggregate model is on the right track. The difference between the Mie-EMT and DDA aggregate fits (band depth and size distribution) can be explained by a simple toy model, described in the next section.

2.3.6 Toy Model

In this section we describe a simple model which helps explain the difference between the DDA and Mie-EMT results, especially in the wavelength region where $n_r \sim 1$. Specifically, the depth of the Christiansen feature is much shallower for the Mie-EMT model than for DDA aggregates, and the size distributions needed to fit the overall shape of the spectrum are different between the two models.

To motivate the model we first separate the net scattering behavior of the particles into

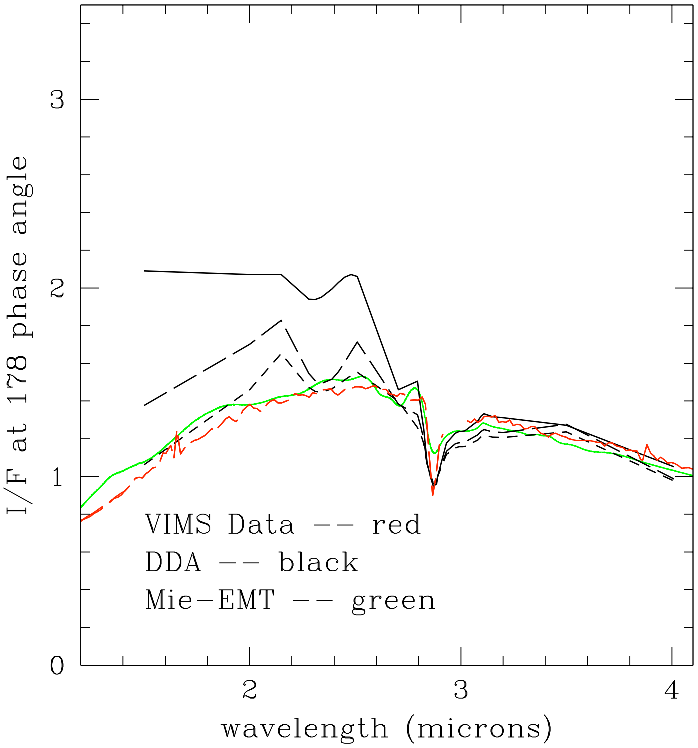

Figure 2.12: F ring VIMS data (red) modelled with: Mie-EMT crystalline ice particles with a power law size distribution ranging between 10-30 μm in radius and 30% porosity (green), DDA crystalline ice aggregates (black) with the same porosity and three different size distributions. The DDA power law size distributions range between 9.5-33 μm in aggregate radii (solid black), 11.5-33 μm (long black dash), and 12.5-33 μm (short dash).

three somewhat differently behaving functions. We rewrite the integrated quantities of equation (6) as

$$\frac{I}{F} = \varpi P \frac{\tau}{4\mu} = \varpi P Q_{ext} \int \pi r^2 n(r) dr, \tag{2.9}$$

where Q_{ext} is also a size-integrated average extinction efficiency. We can separately explore the dependence of ϖ, P, and Q_{ext} on wavelength for any size distribution (figure 2.13). Looking at the components of the scattered field we can see that the extinction efficiency Q_{ext} is the major contributor to the shape of the Christiansen feature, and also has a strong ramp across the wavelength range of interest, while the albedo and phase function dominate the overall shape of the spectrum (its peak near 2-3μm); for this reason, we focus on Q_{ext} to explain the improvement in the fit of the 2.86μm feature in the DDA models.

We next note that Q_{ext} can be related to the phase shift of a wave passing through a particle. These absorbing particles with large x fall under anomalous diffraction theory, and in the range where n_r is close to unity (which also means a small relative phase change $\rho = 2x|n_r - 1| \ll 1$), the extinction efficiency Q_{ext} is a monotonically increasing function of ρ (figure 2.14; see van de Hulst 1957, chapter 11.23). The parameter ρ is a nominal phase difference between a wave traversing a dielectric medium without interfaces and one that has gone the same distance undisturbed. Since Q_{ext} dominates the Christiansen feature (figure 2.13), how fast Q_{ext} increases away from the linear region near $n_r = 1$ or $|m - 1| \approx 0$ where it is a minimum, as wavelength varies, dictates the depth and width of the band. Particles with larger phase shifts have higher Q_{ext} and can remove energy from the incident EM wave more efficiently.

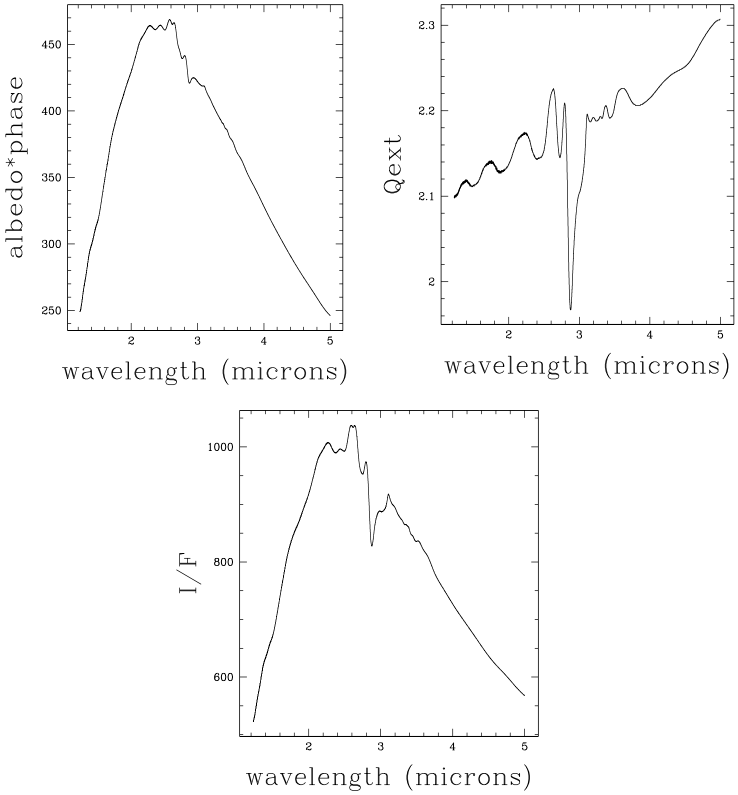

Figure 2.13: I/F is the product of phase function P, extinction coefficient Q_{ext}, and albedo ϖ. The left segment is the product of ϖ and P, with Q_{ext} in the middle, and finally the product of all three parameters giving the normalized intensity I/F in the last segment (plots from Mie-EMT runs). The major effect on the depth of the band in the spectrum is from Q_{ext}.

While ρ is a good general way to parametrize the extinction efficiency (Q_{ext}), the

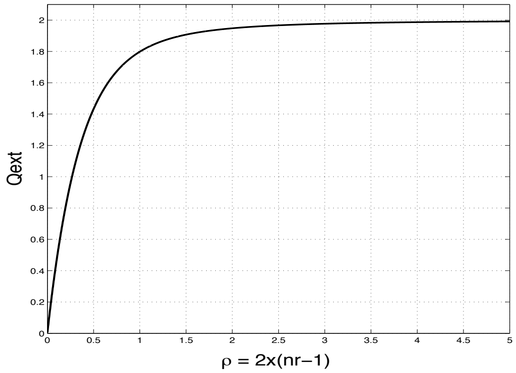

Figure 2.14: Extinction coefficient Q_{ext} versus phase shift $\rho = 2x(n_r - 1)$, where n_r is the real refractive index, and size parameter $x = 2\pi r/\lambda$. The expression used to plot Q_{ext} here is valid in the ADT regime and is for an absorbing particle with $n_r = 1.02$ and $n_i = 0.08$ (values close to those at the Christiansen frequency at 2.86μ). As we approach the Christiansen frequency, $\rho = 2x(n_r - 1) \ll 1$ where Q_{ext} is monatonically increasing .

real phase change through a complicated particle - an aggregate or multilayer - has extra terms related to the phase changes arising from reflection and transmission at the various interfaces. An aggregate with overlapping monomers has many optical interfaces and various pathways of varying lengths for a traveling electromagnetic (EM) wave. We model an aggregate by a dielectric multilayer of ice-vacuum layers with varying thicknesses. Analytical solutions can be written for the complex transmission and reflection coefficients of such multilayers (Born and Wolf 1999, chapters 1 and 14) which include the net phase change of the wave and explicitly identify these interface terms. We vary the thickness and distances between the layers randomly, keeping the aggregate porosity constant by keeping the ratio of the ice to air layers the same for the various configurations. We then average the phase change through many realizations of such multilayers to capture the general behavior of the phase change through an aggregate. A Mie-EMT particle is modeled by a uniform single layer with the EMT optical constants for the desired porosity. Given that the parameter ρ, or relative phase, is a way to characterize the behavior of Q_{ext} for a particle, we estimate the scattering difference between an aggregate and a uniform particle by calculating the phase change of an EM wave traveling through an ice-air multilayer *relative* to a wave passing through a uniform layer of the same total mass.

We calculate the transmission through a multilayer by using the characteristic matrix M for a single layer of thickness z at normal incidence (Born and Wolf 1999). The characteristic matrix of the multilayer M^T is found by multiplying the single layer characteristic matrices

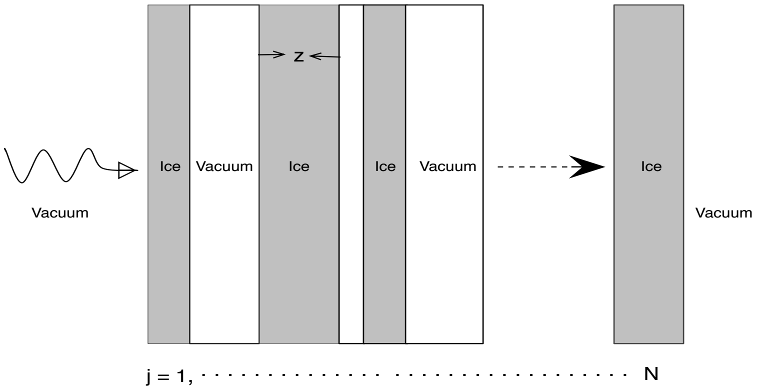

Figure 2.15: Multilayer toy model consists of randomly placed, alternating layers of ice and vacuum with complex refractive index m_j and thickness z_j which can vary randomly between 0-6μm. The total length of the multilayer is kept constant at a value representative of the mean diameter of our aggregate size distribution (about 30μm). We generate many realizations of such multilayers, all having the same average density and total thickness.

(see equations 2.10). The final transmission coefficient t is obtained by calculating the matrix elements of M^T (equation 2.11). The transmission coefficient is the ratio of the transmitted electric field to the incident electric field; it can be written in terms of the phase shift ϕ of the transmitted field after the multilayer $t = |t|\, e^{i\phi}$.

$$M(z_j, m_j) = \begin{vmatrix} M_{11}^j & M_{12}^j \\ M_{21}^j & M_{22}^j \end{vmatrix}; \qquad \begin{matrix} M_{11}^j = M_{22}^j = cos(km_j z_j) \\ M_{12}^j = -\frac{i}{m_j} sin(km_j z_j), \;\; M_{21}^j = -i\, m_j\, sin(km_j z_j) \end{matrix} \tag{2.10}$$

$$M^T = \prod_{j=1}^{N} M(z_j, m_j); \quad t = \frac{2}{(M_{11}^T + M_{12}^T) + (M_{21}^T + M_{22}^T)} \tag{2.11}$$

The difference in phase change between traversal of a multilayer and a single layer is plotted in figure 2.16. The most obvious feature in the phase change of figure 2.16 (at 3.1μm) is not seen in the data, for reasons explained in the caption. Instead, we focus on the more subtle and more interesting behavior near 2.86μm. Note that the phase difference goes through zero where $n_r = 1$, as expected from $\rho = 2x|m - 1|$ (if $n_i \ll 1$). The ice-vacuum multilayer quickly obtains a greater phase shift, moving away from the 2.86 μm Christiansen frequency, relative to a single layer of the same porosity. This more rapidly changing phase difference indicates that Q_{ext} is changing faster for a multilayer, or moving away from $Q_{ext} = 0$ (at $n_r = 1$) faster, than for a single layer. The reason is that the final emergent wave in the multilayer problem has contributions that represent no reflections, two reflections, four reflections, etc (from here on referred to as the "interface terms"). The multireflection cases have larger paths over which to accumulate phase shift. The phase shifts may be larger than 2π, but as you vary the spacings randomly, and average the results, the net effect of adding the multireflection components with random phase shifts is that the net change in phase will be larger for a multilayer than for a solid slab with the same mass/area. At the Christiansen frequency the reflection coefficients get very small; here, the multireflection contribution is negligible so the multislab and single slab cases give the same phase shift. The aggregate also has this "feature" of having multireflection paths in addition to the straight through paths. This will have little effect *at* the Christiansen frequency, but will lead to larger phase shifts close to, and on either side of, the Christiansen frequency. We can conclude that a multilayer representing an aggregate is a better scatterer, and able to diffract more energy at smaller n_r, which is why aggregates have a deeper band. Moreover, the relative phase change also has a greater slope at wavelengths shorter than $\sim 3\mu$m than at longer wavelengths.

This effect also explains why our DDA spectra require different particle size distributions than our Mie-EMT models - the DDA models call for a distribution with fewer small particles (starting around 13 - 30 μm) than the EMT models. Since the smaller aggregates are those which are diffracting into the instrument at the shorter wavelengths, at these high phase angles, and aggregates are better scatterers than uniform particles, fewer of the small aggregates can be allowed for consistency with the data. However at the large wavelength end the scattering properties are similar for aggregates and uniform particles, as we can see in the constant phase difference, because these longer wavelengths blur the interfaces between wavelength-size monomers, causing the "interface" terms to become less important. Thus, for $\lambda > 3\mu$m, the DDA models provide a similar fit to the EMT models with the same size distribution (10 μm - 30 μm).

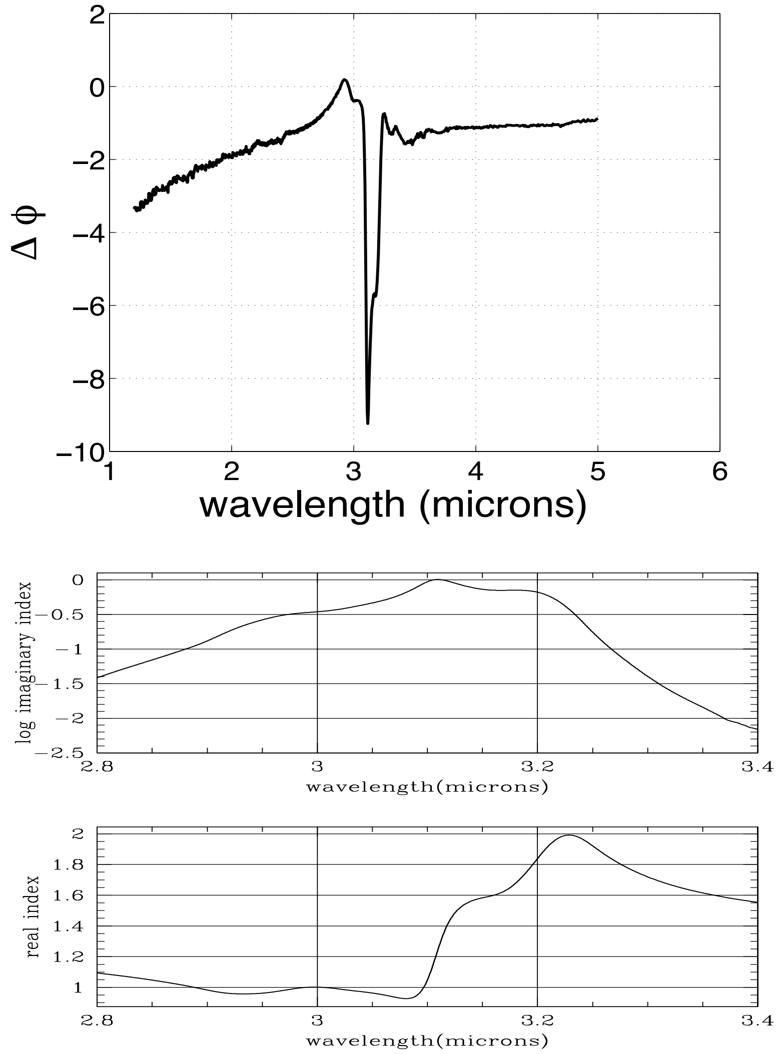

Figure 2.16: (left) Transmitted phase difference $\Delta\phi$ (radians) between an ice-air multilayer and single ice layer with 30% porosity and 30μ thickness versus λ (μm). There are three main features in this plot: (1) the phase difference sharp rise and fall about 2.86μm is where the transmitted EM wave accumulates a larger phase change after going through the multilayer interfaces compared to a single layer (see section 3.5); (2) the asymmetric slope of the phase change below and above $\sim 3\mu$m affects the size distribution used in the DDA model (represented by a multilayer) compared to that used in the Mie-EMT model (represented by a single layer) (see section 3.5); and finally (3) another large accumulation of phase change is at 3.1μm where the interfaces of a multilayer play a large role due to the large imaginary index at this wavelength (see right panels for optical constants). However, we don't see this feature in the observed spectrum because the particles are absorbing with a large imaginary index and Q_{ext} never gets small. That is, the energy transmitted thru the particle is negligible and its effects are insensitve to the details of its phase shift, as opposed to the phase-shift-sensitive behavior at the Christiansen frequency where the energy transmitted is significant.

2.4 Conclusion

Our Mie-EMT modeling has restricted the particle size distribution to a limited range between $10 - 30\mu$m. Further tests can be done to investigate the exact nature of the rolloff at the limits of the size distribution, but for our purposes an estimate of the size range is enough to get the general profile of the spectra. Our modeling has also constrained the particle composition using the wavelength of the central dip in the spectrum, which is very sensitive to composition at high phase angles. We found that crystalline ice best captures the position of the central dip, as opposed to amorphous ice which shows a dip at a shorter wavelength than observed. Diffraction dominates the overall spectral shape, and the only spectral feature that shows up is at the Christiansen frequency where the real part of the refractive index goes through unity and the imaginary part remains very small, so the particles' optical activity is drastically reduced. We further explored the possibility of aggregates by using the DDA approach and found that aggregates with a size distribution similar to the Mie-EMT models provide a better fit for the depth and width of the central band. The two modeling approaches imply slightly different size distributions, which can be explained by a simple dielectric multilayer toy model. Aggregates are more effective scatterers than uniform particles, and hence have a deeper 2.86μm band and asymmetric spectral shape. This is because of the many surface-interface reflections which become more important at shorter wavelengths and higher refractive indices. Another implication is that no other material besides water ice can be present with a significant fractional abundance, because no other common material has $n_r = 1$ at 2.86μm. This confirms that crystalline water ice must be the dominant component in the F ring particles. However, more detailed modeling on better data might constrain small amounts of non-icy pollutants such as silicates.

2.5 Acknowledgements

We are very grateful to Kathy Rages for providing her Mie scattering code and for assistance fixing problems it developed with the unusual set of refractive indices we were using. Also, we'd like to thank Terry Nelson, Piyush Mehrotra, and especially Art Lazanoff for help getting the optimzing done, Denis Richard for his help testing the code, Rachel Mastrapa for providing data in advance of publication and several helpful conversations, observation designers on the VIMS team, Essam Marouf and Frank Bridges for insightful conversations. The research was partially supported by the Cassini project and partially by a grant to JNC from NASA's Planetary Geology and Geophysics program.

2.6 References

Arnott, W. P., Y. Y. Dong, J. Hallett, (1995). Extinction efficiency in the infrared (218 μm) of laboratory ice clouds: observations of scattering minima in the Christiansen bands of ice. Applied Optics, Vol. 34, Issue 3, pp. 541-551.

Bertie, J. E., S. M. Jacobs, (1977). Far-infrared absorption by ices Ih and Ic at 4.3 K and the powder diffraction pattern of ice Ic. J. Chem. Phys. 67, pp. 2445.

Bertie, J. E., (1969). Absorptivity of Ice I in the range 4000-30 cm^{-1}. J. Chem. Phys. 50, pp. 4501.

Barbara, J. M., L. W. Esposito, (2002). Moonlet collisions and the effects of tidally modified accretion in Saturn's F Ring. Icarus 160, Issue 1, pp. 161-171.

Bosh, A. S., C. B. Olkin, R. G. French, P. D. Nicholson, (2002). Saturn's F Ring: Kinematics and particle sizes from stellar occultation studies. Icarus Volume 157, Issue 1, pp. 57-75.

Bosh, A. S., A. S. Rivkin, J. W. Percival, M. Taylord, G. W. van Citterse, (1997). Saturn ring-plane crossing, May 1995: pole precession and ring thickness. Icarus 129, 2, pp. 555-561.

Bohren, C. F., D. R. Huffman, (1983). Absorption and scattering of light by small particles. Wiley, New York.

Born, M., E. Wolf, (1999). Principles of optics, seventh edition. Cambridge University Press.

Brown, R. H., K. H. Baines, G. Bellucci, J. P. Bibring, B. J. Buratti, F. Capaccioni, P. Cerroni, R. N. Clark, A. Coradini, D. P. Cruikshank, P. Drossart, V. Formisano, R. Jaumann, Y. Langevin, D. L. Matson, T. B. Mccord, V. Mennella, E. Miller, R. M. Nelson, P. D. Nicholson, B. Sicardy, C. Sotin, (2004). The Cassini Visual And Infrared Mapping Spectrometer (VIMS) investigation. Space Science Reviews 115, pp. 111-168.

Clark, R., and 26 other authors, (2009). The Composition of Saturn's Rings: Results from Cassini VIMS, Icarus, submitted. (Roger - need a better reference with authors)

Conel, J. E., (1969) Infrared emissivities of silicates: experimental results and a cloudy atmosphere model of spectral emission from condensed particulate mediums. J. Geophys. Res., 74, pp. 1614-1634.

Charnoz, S., C. C. Porco, E. Deu, A. Brahic, J. N. Spitale, G. Bacques, K. Baillie, (2005). Cassini Discovers a Kinematic Spiral Ring Around Saturn. Science 310. no. 5752, pp. 1300 - 1304.

Cuzzi, J. N., (1985). Rings of Uranus - not so thick, not so black. Icarus 63, Issue 2, pp. 312-316.

Cuzzi, J. N., J. A. Burns, (1988). Charged particle depletion surrounding Saturn's F ring: Evidence for a moonlet belt?. Icarus 74, Issue 2, pp. 284-324.

Cuzzi, J., R. Clark, G. Filacchione, R. French, R. Johnson, E. Marouf, L. Spilker, (2009). Ring Particle Composition and Size Distribution; in ”The Saturn system after Cassini-Huygens”; M. Dougherty, R. Brown, and H. Waite, eds; Springer.

Cuzzi, J. N., P. R. Estrada, (1998). Compositional evolution of Saturn's rings due to meteoroid bombardment. Icarus 132, Issue 1, pp. 1-35.

Draine, B. T., and K. Allaf-Akbari, (2006). X-ray scattering by nonspherical grains. I. oblate spheroids. The Astrophyscial Journal 652, pp. 1318-1330.

Draine, B. T., P. J. Flatau, (1994). Discrete dipole approximation for scattering calculations. J. Opt. Soc. Am. 11, pp. 1491-1499.

Esposito, L. W., Cuzzi, J. N., Holberg, J. B., Marouf, E. A., Tyler, G. L., Porco, C. C., (1984). Saturn's rings - Structure, dynamics, and particle properties. In: Saturn University of Arizona Press, pp. 463-545.

Hansen, J. E., and L. D. Travis, (1974). Light scattering in planetary atmospheres. Space Science Reviews 16, pp. 527-610.

Hedman, M. M., P. D. Nicholson, M. R. Showalter, R. H. Brown, B. J. Buratti, R. N. Clark, (2009). Spectral Observations of the Enceladus plume with Cassini-VIMS. ApJ 693, pp. 1749-1762.

Hornig, D. F., H. F. White, F. P. Reding, (1958). The infrared spectra of crystallline H_2O, D_2O and HDO. Spectrochimica Acta 12, pp. 338-349.

Hudgins, D. M., S. A. Sandford , L. J. Allamandola, A. G. Tielens, (1993). Mid- and far-infrared spectroscopy of ices - Optical constants and integrated absorbances. Astrophysical Journal Supplement Series vol. 86, no. 2, pp. 713-870.

Lane, A. L., C. W. Hord, R. A. West, L. W. Esposito, D. L. Coffeen, M. Sato, K. E. Simmons, R. B. Pomphrey, R B. Morris, (1982). Photopolarimetry from Voyager 2; Preliminary Results on Saturn, Titan, and the Rings. Science 215, no. 4532, pp. 537 - 543.

Leger, A., S. Gauthier, D. Defourneau, D. Rouan, (1983) Properties of amorphous H2O ice and origin of the 3.1-micron absorption. Astronomy and Astrophysics, vol. 117, no. 1, pp. 164-169.

Mastrapa, R. M., S. A. Sandford, T. L. Roush, D. P. Cruikshank, C. M. Dalle Ore, (2009). Optical Constants of amorphous and crystalline H2O-ice: 2.5-22 μm (4000-455 cm^{-1}). ApJ 701, pp. 1347-1356.

Mastrapa, R. M., M.P. Bernstein, S.A. Sandford, T.L. Roush, D.P. Cruikshank, C.M. Dalle Ore, (2008). Optical constants of amorphous and crystalline H2O-ice in the near infrared from 1.1 to 2.6 m. Icarus 197, Issue 1, pp. 307-320.

McCord, T.B., A. Coradini, C.A. Hibbitts, F. Capaccioni, G.B. Hansen, G. Filacchione, R.N. Clark, P. Cerroni, R.H. Brown, K.H. Baines, G. Bellucci, J. P. Bibring, B.J. Buratti, E. Bussoletti, M. Combes, D.P. Cruikshank, P. Drossart, V. Formisano, R. Jaumann, Y. Langevin, D.L. Matson, R.M. Nelson, P.D. Nicholson, B. Sicardy, C. Sotin, (2004). Cassini VIMS observations of the Galilean satellites including the VIMS calibration procedure. Icarus 172, Issue 1, pp. 104-126.

Murray, C. D., K. Beurle, N. J. Cooper, M. W. Evans, G. A. Williams, S. Charnoz, (2008). The determination of the structure of Saturn's F ring by nearby moonlets. Nature 453, pp.

739-744

Murray, C. D., M. K. Gordon, S. M. Giuliatti Winter, (1997). Unraveling the Strands of Saturn's F Ring. Icarus 129, Issue 2, pp. 304-316.

Mustard, J. F., J. E. Hays, (1997). Effects of Hyperfine Particles on Reflectance Spectra from 0.3 to 25 microns. Icarus 125, pp. 145163.

Nash, D. B., J. W. Salibury, J. E. Conel, P. G. Lucey, P. R. Christensen, (1993). Evaluation of Infrared Emission Spectroscopy for Mapping the Moon's Surface Composition From Lunar Orbit. J. Geophysical Research, VOL. 98, NO. El2, pp. 23,535-23,552.

Nicholson, P. D., R. G. French, E. Tollestrup, J. N. Cuzzi, J. Harrington, K. Matthews, O. Perkovi, R. J. Stoverg, (2000) .Saturn's Rings I: Optical depth profiles from the 28 Sgr occultation. Icarus 145, Issue 2, pp. 474-501.

Nicholson, P. D., M. M. Hedman, R. N. Clark, M. R. Showalter, D. P. Cruikshank, J. N. Cuzzi, G. Filacchione, F. Capaccioni, P. Cerroni, G. B. Hansen, B. Sicardy, P. Drossart, R. H. Brown, B. J. Buratti, K. H. Baines, A. Coradini, (2008). A close look at Saturn's rings with Cassini VIMS. Icarus 193, Issue 1, pp. 182-212.

Nicholson, P. D., Hedman, M. M., Wallis, B. D., (2007). Cassini-VIMS Team Cassini-VIMS Observations of stellar occultations by Saturn's rings. AAS/DDA meeting 38, 12.05.

Ockman, N., (1958). The Infra-Red and Raman spectra of Ice. Adv. Physics, 7.

Pollack, J. B., J. N. Cuzzi, (1980). Scattering by Nonspherical Particles of Size Comparable to a Wavelength: A new semi-empirical theory and its application to tropospheric aerosols. Journal of the Atmospheric Sciences 37, Issue 4, pp. 868881.

Poulet, F., D. P. Cruikshank, J. N. Cuzzi, T. L. Roush, R. G. French, (2003). Compositions of Saturn's rings A, B, and C from high resolution near-infrared spectroscopic observations. Astronomy and Astrophysics 412, pp. 305-316.

Purcell, E. M., C. Pennypacker, (1973). Scattering and absorption of light by nonspherical dielectric grains. Astrophys. J. 186, pp. 705-714.

Scargle, J., J. N. Cuzzi, A. Dobrovolskis, L. Dones, R. Hogan, C. Levit, M. Showalter, K. Young, (1993). Dynamical Evolution of Saturn's Rings. AAS meeting 25, 26.04.

Shen, Y., B. T. Draine, E. T. Johnson, (2008). Modeling porous dust grains with ballistic aggregates I: Geometry and optical properties. Astrophys.J. 689, pp. 260-275.

Showalter, M. R., J. N. Cuzzi, S. M. Larson, (1991). Structure and particle properties of Saturn's E Ring. Icarus 94, Issue 2, pp. 451-473.

Showalter, M. R., R. French, R. Sfair, C. Argelles, M. Pajuelo, P. Becerra, M. Hedman, and P. Nicholson (2009). The Brightening of Saturn's F Ring; 2009 DPS meeting.

Showalter, M. R., J. A. Burns, (1982). A numerical study of Saturn's F-ring. Icarus 52, Issue 3, pp. 526-544.

Showalter, M. R., J. B. Pollack, M. E. Ockert, L. R. Doyle, J. B. Dalton, (1992). A photometric study of Saturn's Ring. Icarus 100, Issue 2, pp. 394-411.

Smith, B. A., L. Soderblom, R. Beebe, J. Boyce, G. Briggs, A. Bunker, S. A. Collins, C. J. Hansen, T. V. Johnson, J. L. Mitchell, R. J. Terrile, M. Carr, A. F. Cook II, J. Cuzzi, J. B. Pollack, G. E. Danielson, A. Ingersoll, M. E. Davies, G. E. Hunt, H. Masursky, E. Shoemaker, D. Morrison, T. Owen, C. Sagan, J. Veverka, R. Strom, V. E. Suomi, (1981). Encounter with Saturn: Voyager 1 imaging science results. Science. 212, no. 4491, pp. 163 - 191.

Smith B. A., L. Soderblom, R. Batson, P. Bridges, J. Inge, H. Masursky, E. Shoemaker, R. Beebe, J. Boyce, G. Briggs, A. Bunker, S. A. Collins, C. J. Hansen, T. V. Johnson, J. L. Mitchell, R. J. Terrile, A. F. Cook II, J. Cuzzi, J B. Pollack, G. E. Danielson, A. P. Ingersoll, M. E. Davies, G. E. Hunt, D. Morrison, T. Owen, C. Sagan, J. Veverka, R. Strom, V. E. Suomi, (1982). A new look at the Saturn system: The Voyager 2 images. Science. 215., no. 4532, pp. 504 - 537.

Throop, H.B., L. W. Esposito, (1998). G ring particle sizes derived from ring plane crossing observations. Icarus, 131, Issue 1, pp. 152-166.

Tyler, G. L., E. A. Marouf, R. A. Simpson, H. A. Zebker, V. R. Eshleman, (1983). The microwave opacity of Saturn's rings at wavelengths of 3.6 and 13 cm from Voyager 1 radio occultation. Icarus 54, Issue 2, pp. 160-188.

Van de Hulst, H. C., (1957). Light scattering by small particles. Wiley, New York.

Winter, O. C., D. C. Mouro, S. M. Giuliatti Winter, F. Spahn, C. da Cruz, (2007). Moonlets wandering on a leash-ring. Monthly notices of the Royal Astronomical Society 380, Issue 1, pp. L54 - L57.

Chapter 3

Regolith radiative transfer model

3.1 Background

This section describes a new approach to modeling radiative transfer in granular surfaces, referred to as regoliths. This model is based on the discrete dipole approximation (DDA) where scattering calculations are not limited by packing density, shape, or size of particles in the regolith. Regolith scattering can be categorized by two major optical regimes defined by the refractive indices of the regolith material. The first regime is referred to as "surface scattering" (where real and/or imaginary indices, and surface reflectance are large). The second regime is "volume scattering" (where the imaginary index is low and the real index is greater than or close to 1) which has moderate surface reflectance and low internal absorption. Restrahlen bands fall into the first category and "transparency regions" including the Christiansen feature (where the real index $n = 1$) fall into the second (Mustard and Hays 1997, MH97). Mineral identification and grain size estimation is accomplished from remote sensing data using the shapes and relative strengths of these strong bands, and it is in these strong bands and the transparency regions between them where the shortcomings of standard theoretical models are the most apparent. In a general way, the variations of these different feature strengths with regolith grain size variations are somewhat in accord with simple predictions; however, at a closer look, the correspondence is poor, as shown by Moersch and Christensen (MC95) for granular silicates with well known composition and size distribution. Furthermore, MH97 show that the asymmetry of the Olivine restrahlen bands at 9-11μm wavelength is opposite that of theoretical predictions. For quartz, MH97 and MC95 both show that strong restrahlen bands are poorly modeled in yet another way, with theoretical models showing almost no variation with regolith grain size and data showing noticeable variation. These are the high-refractive-index "surface scattering" regimes. Differences are easily found in the "volume scattering" transparency regimes as well: MH97 show that the sense of the observed 10-12μm band strength variation, as grain size varies between 2-60μm, is directly opposite the sense predicted by the models in figure 3.1.

As an example we tested the performance of some typical popular models against laboratory measurements of emissivity from a layer of quartz grains for various grain sizes (data courtesy P. Christensen and J. Michalski). The test models used a combination of Mie/Conel theory (MC95) to calculate single grain albedo and van de Hulst's similarity relations to calculate an integrated emissivity (Cuzzi and Estrada 1998). As we can see in figure 3.1, the Mie-Conel-van de Hulst models predict some of the structure in the quartz emissivity spectrum, but miss other major features. Also, the discrepancy increases for smaller wavelength-size grains at larger wavelengths which starts getting into the region of interest for our applications. Note also, in figure 3.1 (and in MC95), the 20-22 μm spectra show entirely different behavior in the Mie-Conel theoretical models than in the data of Michalsky and Christiansen, in a way distinct from surrounding wavelength regions.

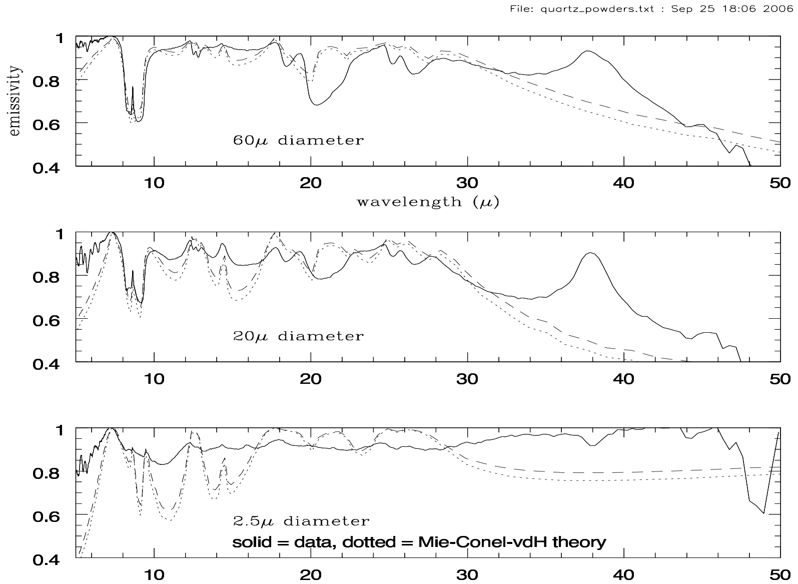

Figure 3.1: Comparison of Mie-Conel and van De Hulst models (dashed and dotted lines) with laboratory emissivity measurements of granular quartz layer (solid line) for three separate grain size

To recap, current models do not handle key physical properties of regolith surfaces (close packing, irregular particles, wavelength size grains) from first principles and fail to capture many important features of laboratory silicate data and remote observations of planetary surfaces. Our model is based on the Discrete Dipole Approximation (DDA) which accounts for closely packed irregular grains of arbitrary size. Our model will have applications to reflectance and emission spectroscopy of grainy regoliths in general (Mars, the moon, asteroids, etc) at mid- and far-infrared wavelengths.

The DDA calculates the scattering and absorption of electromagnetic waves by a target object of arbitrary geometry and thereby automatically accounts for all close packing effects and size dependence. In the DDA approach, target objects are modeled as a regular lattice of individual polarizable dipoles with size smaller than a wavelength. The polarizability of each dipole can be adjusted to represent the refractive index of an arbitrary material (Drain Flatau 1994,1988). Heterogeneous composition and irregular shape are easily captured this way.

To apply the DDA approach to a regolith layer, we have made several changes from the normal way it has been used. In one novel modification, horizontally extended, semi-infinite slabs of regolith made up of closely packed grains of arbitrary size and shape are modeled using a single target 'unit cell' subject to periodic horizontal boundary condition (PBC). In a second novel modification, the emergent intensities are calculated in the near field of the layer. This is a new approach to calculating scattering using the DDA method since traditionally all scattering calculations have been done in the far field. This step itself has two parts: evaluating the scattered electric field on a planar 2-D grid, and evaluating the hemispherical angular intensity distribution using a fourier transform approach.

In section 3.2 we describe our approach in its three main elements: (1) a DDA code with horizontal periodic boundary conditions, (2) calculating the scattered field in the near field of the layer, and (3) determining the angular direction of the emitted radiation using a Fourier analysis method. In section 3.3, we present the tests we have run to evaluate the performance of our model against analytical results for transmission, and reflection, from a homogeneous dielectric layer, finding good agreement. In section 3.3.2 we present our model of granular layers of various porosities.

3.2 Model description

The DDA uses a regular lattice structure composed of closely spaced independently scattering dipoles to represent targets of various composition. An important criterion for the dipole lattice is that the size of and spacing (both given by d) between the dipoles must be small compared with the wavelength $\lambda = \frac{2\pi}{k}$ of the incident radiation in the target material: $|M|kd < \frac{1}{2}$, where M is the complex refractive index of the target . The second criterion is that for a given d, the total number of dipoles N must be large enough to describe the shape of the target and its constituent monomers satisfactorily. To model extended layers we use the same validity criterion as for finite targets, but add periodic horizontal boundary conditions to replicate our finite unit cell and represent a layer of infinite horizontal extent.

3.2.1 Periodic boundary conditions

A finite rectangular slab of dipoles, referred to as the target unit cell (TUC), is periodically replicated on the horizontal plane to represent a semi-infinite 3-D layer. Each dipole in the TUC has an image dipole in each periodic replica cell. All dipoles in the TUC and replica oscillate with the appropriate phases in response to an incident plane wave. The electromagnetic field inside the target is the sum of the initial radiation and the field from all other dipoles in the layer. A steady state solution is obtained by an iterative method, as described below. The dipoles are located at positions $\mathbf{r} = \mathbf{r}_{jmn}$ with the indices m, n running over the replica targets, and j running over the dipoles in the TUC:

$$\mathbf{r}_{jmn} = \mathbf{r}_{j00} + mL_y\hat{y} + nL_z\hat{z} \tag{3.1}$$

where L_y, L_z are the lengths of the TUC in each dimension. The incident E field is.

$$\mathbf{E}_{inc} = \mathbf{E}_0 e^{ik\cdot\mathbf{r}-iwt} \tag{3.2}$$

The polarizations of the dipoles $\mathbf{P}_{jmn}$ are initially driven by the incident field, and phase shifted relative to the TUC polarization $\mathbf{P}_{j00}$:

$$\mathbf{P}_{jmn} = \alpha_j\mathbf{E}_{inc}(r_j, t) = \alpha_j\mathbf{E}_0 e^{ik\cdot(\mathbf{r}_{j00}+mL_y\hat{y}+nL_z\hat{z})-iwt} = \mathbf{P}_{j00}e^{ik(\mathbf{r}_{jmn}-\mathbf{r}_{j00})} \tag{3.3}$$

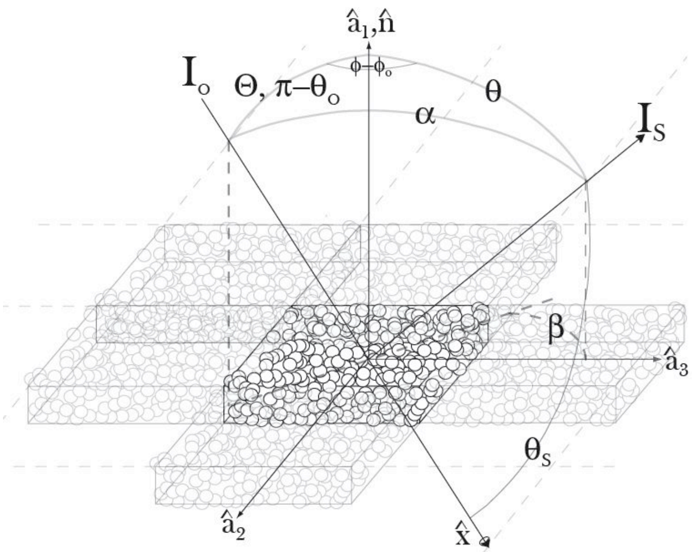

Figure 3.2: Schematic of the DDA code operated in the PBC regime, with the TUC shown in the center and image cells arrayed around. I_o indicates the incident flux and I_s indicates the scattered flux. θ is the angle between the incidednt beam and normal axis of the particle layer and ϕ is the azimuthal rotation around the normal of the layer.

The field at position j in the TUC $(m = n = 0)$ is due to all other dipoles both in the TUC (index l) and in the replica cells.

$$\mathbf{E}_{j00} = -\mathbf{A}_{jlmn}\left[\mathbf{P}_{l00}e^{ik(\mathbf{r}_{jmn}-\mathbf{r}_{j00})}\right] = -\mathbf{A}_{jlmn}e^{ik(\mathbf{r}_{jmn}-\mathbf{r}_{j00})}\mathbf{P}_{l00} \tag{3.4}$$

$$\mathbf{E}_{j00} = -\mathbf{A}_{jl}^{PBC}\mathbf{P}_{l00}, \quad \mathbf{A}_{jl}^{PBC} = \mathbf{A}_{jlmn}e^{ik(\mathbf{r}_{jmn}-\mathbf{r}_{j00})} \tag{3.5}$$

Once the matrix $\mathbf{A}_{j,k}^{PBC}$ has been calculated, then the polarization $\mathbf{P}_{j00}$ for each dipole in the TUC can be calculated using an iterative technique.

$$\mathbf{P}_{j00} = \alpha_j\left[\mathbf{E}_{inc}(r_j) - \sum_l \mathbf{A}_{j,l}^{PBC}\mathbf{P}_{l00}\right] \tag{3.6}$$

3.2.2 Calculating radiation from the PBC dipole layer

Once the polarization of the dipoles in the target layer has been obtained, we can calculate the radiated field. For most purposes in the past, the radiated field was calculated in the far field of the target $(kr >> 1)$; however, this introduced edge effects since the radiation was calculated by summing over the radiated contributions only from a single TUC. This problem will be present even if we were to include more TUC's; no matter how large the target, its finite size will be manifested in the far radiation field as an increasingly narrow diffraction-like feature. Another problem with calculating radiation in the far field is that eventually we would like to build thicker granular layers by placing DDA layers next to each other and using an adding/doubling code to calculate the resultant scattered field. For this application, the far field limit does not apply and we have to move closer to the layer to sample the radiation field.

3.2.2.1 The nearfield

Given that the DDA layers are placed close to each other to represent a regolith, we need the radiated field in close proximity of the layer that is, in its near field. This region is known as the shadow of the layer. Since we can't make any approximations in the shadow we will use the full Green's function to calculate the radiated field (see below), which is a sensitive function of position with respect to the layer. In the horizontal y and z directions the phase of the field fluctuates rapidly. In the x direction, as the field travels away from the layer it transitions from the near field (where evanescent waves can be present) to the Fresnel zone where patches of dipoles within the target are oscillating coherently, and finally to the far field limit where the semi-infinite layer is seen as a finite target.

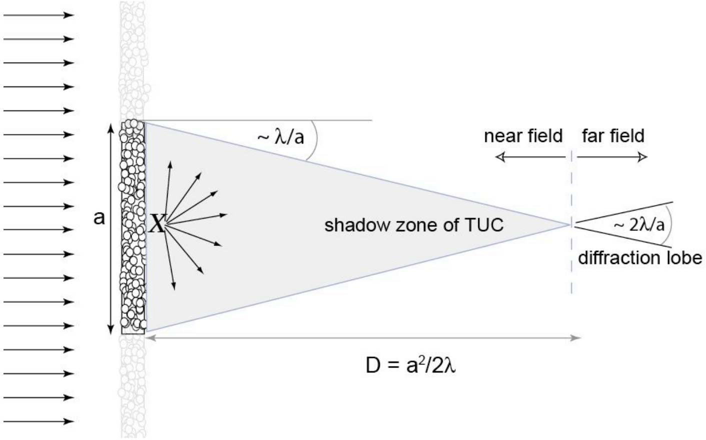

Figure 3.3: Schematic of our approach to determining T in the shadow zone of the TUC. The diffuse reflectivity, will be determined in a similar geometry on the lit side of the TUC.

3.2.2.2 Sampling the field on a 2-D sheet

In the next two sections we will show how we go from the field sampled on a two dimensional grid parallel to a layer, to a full three dimensional angular distribution in elevation and azimuth relative to the layer normal. The first step in obtaining the scattered intensity within the classical shadow zone of the slab, is to calculate the scattered electric field on a 2-D grid (otherwise known as the target unit radiance or TUR) just outside the layer. We will use the image cells in calculating the field within the TUR; since the dipole polarizations $\mathbf{P}_j$ in the TUC are periodic, the TUR field is also periodic. The general expression for the field due to a collection of dipoles with polarization $\mathbf{P}_j$ of the jth dipole is as follows:

$$\mathbf{E}_{TUR} = k^2 \sum_{j=1}^{N} \mathbf{P_j} \cdot \tilde{\tilde{\mathbf{G}}}, \tag{3.7}$$

$$\tilde{\tilde{\mathbf{G}}} = \frac{e^{ikr_{jk}}}{r_{jk}} \left(k^2 (\hat{r}_{jk}\hat{r}_{jk} - \tilde{\tilde{\mathbf{I}}}) + \frac{ikr_{jk} - 1}{r_{jk}^2} (3\hat{r}_{jk}\hat{r}_{jk} - \tilde{\tilde{\mathbf{I}}}) \right), \tag{3.8}$$

wherer_j = distance to grid points in the TUC,r_k = distance to grid points in the TUR, $r_{jk} = |\vec{r}_j - \vec{r}_k|$, $\hat{r}_{jk} = (\vec{r}_j - \vec{r}_k)/r_{jk}$, $\tilde{\tilde{\mathbf{I}}}$ is the identity tensor, and $\tilde{\tilde{\mathbf{G}}}$ is the free space tensor Green's function. This is done on both sides of the slab, *i.e.*, on the reflected and transmitted sides. On the transmitted side, we will add the incident electric field that is propagating through the slab. However, on the reflected side we will only calculate the scattered field. This method has been written as a FORTRAN code called DDFIELD which is currently distributed with ddscat as a subroutine. The layer polarizabilities calculated by ddscat are fed into DDFIELD to calculated the electric field from them.

3.2.3 Determining the angular distribution of scattered intensity

Our approach to determining the emergent intensities in the near field, as a function of angle θ, ϕ for any given θ_o, ϕ_o, follows the formalism of Mandel and Wolf (1994). It is well known that a complex field distribution can be represented by a superposition of simpler plane waves. Now, if the complex waveform is decomposed across a plane, then the spatial components represent plane waves traveling away from the plane in various angular directions. Consider a monochromatic wave-field $\mathbf{E}(x, y, z)$ that satisfies the Helmholtz equation across a plane $x = x_0$. and that can also be represented by a Fourier integral.

$$\mathbf{E}_{TUR} = \mathbf{E}(y, z : x_0) = \int\int \mathbf{E}(k_y, k_z : x_0) e^{i(k_y y + k_z z)} dk_y dk_z \tag{3.9}$$

Then the field $\mathbf{E}(x, y, z)$ has the following inverse transform:

$$\mathbf{E}(k_y, k_z : x_0) = \int\int \mathbf{E}(y, z : x_0) e^{i(k_y y + k_z z)} dy dz \tag{3.10}$$

The Helmholtz equation is:

$$(\bigtriangledown^2 + k^2)\mathbf{E}(\mathbf{r}) = 0, \text{where } \ \mathbf{r} = (x, y, z) \tag{3.11}$$

Substituting the 2-D Fourier integral of the field $\mathbf{E}(x, y, z)$ into the Helmholtz equation we get the differential equation:

$$\frac{\partial^2 \mathbf{E}(y, z : x_0)}{\partial x^2} + k_x^2 \mathbf{E}(y, z : x_0) = 0 \tag{3.12}$$

with the general solution:

$$\mathbf{E}(k_y, k_z : x_0) = A(k_y, k_z) e^{ik_x x_0} + B(k_y, k_z) e^{-ik_x x_0} \tag{3.13}$$

$$k_x^2 = k^2 - k_y^2 - k_z^2, \quad k = \frac{2\pi}{\lambda} \tag{3.14}$$

$$k_x = (k^2 - k_y^2 - k_z^2)^{\frac{1}{2}} \ \text{ where } \ k_y^2 + k_z^2 \leq k^2 \tag{3.15}$$

$$k_x = i(k_y^2 + k_z^2 - k^2)^{\frac{1}{2}} \tag{3.16}$$

The roots with $k_y^2 + k_z^2 > k^2$ are evanescent and will decay. Therefore we will sample the field in a position where the evanescent terms have decayed and are negligible (as determined by tests). We would like to compute the scattered field emanating away from the target, therefore we will only consider the solution in a half space: in the reflected region $x < 0$, $B(k_y, k_z) = 0$ and in the transmitted region $x > 0$, $A(k_y, k_z) = 0$. We can proceed with one side since the other differs by a minus sign. For example on the transmitted side we can write the Fourier transform of the electric field across any plane $x = x_0$ as follows:

$$\mathbf{A}(k_y, k_z)e^{ik_x x_0} = \int\int \mathbf{E}(x_0, y, z)e^{i(k_y y + k_z z)}dk_y dk_z \tag{3.17}$$

where the scattered electric field $\mathbf{E}(x_0, y, z)$ has been computed on a grid of points on a plane $x = x_0$ in the shadow zone (the TUR). The Fourier transform of the electric field on the TUR gives the relative strength of each spatial frequency component composing that field, and therefore each plane wave stream leaving the TUR. The distribution of energy as a function of spatial frequency $k = 2\pi/\lambda$ should be highly localized at k^2, allowing us to determine $k_x^2 = k^2 - k_y^2 - k_z^2$ and its angular distribution is the angular distribution of the emergent scattered intensity at the plane $x = x_0$. This approach will also provide a way to discriminate against any static components in the field; appearance of significant anomalous energy at high spatial frequencies (*i.e.* much higher than $|\vec{k}|$), is an indication of static fields. If this problem appears, we would merely move the TUR slightly further from the face of the TUC.

3.2.3.1 Fourier transform method and sampling relationships

As described in section 3.2.2.2, subroutine DDFIELD is used to determine the electric field $E(x_0; y, z)$ on a 2D grid located a distance x_o away from the layer equation 3.7 and 3.8. The sampling location x_0 is adjustable within the shadow zone (the near field of the layer), but should not be so close as to improperly sample evanescent or non-propagating field components from individual grains. Incident wave polarizations can be either parallel or perpendicular to the scattering plane (the plane containing the mean surface normal $\mathbf{e}_x$ and the incident beam). At each incident zenith angle θ_0, calculations of $E(x_0; y, z)$ are made for many azimuthal orientations, defined by the angle β and several regolith particle realizations, and averaged incoherently (in intensity space). Such averaged results can then be obtained at a number of zenith angles θ_0, and used to obtain the full diffuse scattering function $S(\tau; \mu_0, \mu, \phi - \phi_0)$ and diffuse transmission function $T(\tau; \mu_0, \mu, \phi - \phi_0)$ of a layer with optical depth τ and emission angle $\mu = cos\theta$. As noted by Hansen (1969) the quantities $S(\tau; \mu_0, \mu, \phi - \phi_0)$ and $T(\tau; \mu_0, \mu, \phi - \phi_0)$ can be thought of as suitably normalized intensities; thus our fundamental goal is to determine the intensities diffusely scattered and transmitted by our layer of grains.

We use the formalism of the *angular spectrum*, described by Mandel and Wolf (1994, section 3.1.2). The angular spectrum and the field on a grid are usually defined as infinite-domain Fourier transform pairs (see below). We will use the "cycles" definition of frequency (in our case, spatial frequency) rather than the "radians" definition used by Mandel and Wolf (MW) for simplicity; this removes floating factors of $(1/2\pi)$. We will retain the transform "direction" notation of MW, which is common (see also Blackman and Tukey method in Stoica and Moses 1997, SM97); in this convention the frequency-dependent function is obtained using the negative exponential. We note that Numerical Recipes (Press et al. 1999) adopts the opposite "direction" convention, which we feel leads to less intuitive results in the frequency domain. In the 1D case, with y spatial, and k and spatial frequency, coordinates respectively, the infinite Fourier Transform reads:

$$g(k) = \int_{-\infty}^{\infty} f(y) e^{-2\pi i y k} dy \tag{3.18}$$

$$f(y) = \int_{-\infty}^{\infty} g(k) e^{2\pi i y k} dk \tag{3.19}$$

MW and other authors discuss the angular spectrum only in the context of the infinite Fourier Transform shown above, where the dimensions of $f(y)$ and $g(k)$ are different, but for practical reasons we will be using discrete or finite Fourier Transforms. This leads to subtle but important differences. In particular, changing to the *finite* transform pairs $f(y)$ and $a(k) = g(k)/L$ and then expressing them in their discrete series forms leads to:

$$a(k) = g(k)/L = \frac{1}{L} \int_{-L/2}^{L/2} f(y) e^{-2\pi i y k} dy \approx \frac{1}{N \Delta y} \sum_{l} f(y_l) e^{-2\pi i y_l k} \Delta y, \quad , \tag{3.20}$$

or, now also discretizing k:

$$a(k_\alpha) = \frac{1}{N} \sum_{l} f(y_l) e^{-2\pi i l \alpha / N} \tag{3.21}$$

$$f(y_l) = \sum_{\alpha} a(k_\alpha) e^{2\pi i l \alpha / N} \tag{3.22}$$

where $y_l = l\Delta y$, $k_\alpha = \alpha \Delta k$, and $\Delta k = 1/(N\Delta y)$ where N is the number of points in both the y and k arrays. Note that the dimensions of $f(y)$ and $a(k)$ are the same. This convention seems to be the more common one, in that the prefactor goes with the negative sign in the exponential, and the negative sign is used to generate the function defined in frequency space (SM97).

We thus trivially rewrite the transform pair of MW, using their equations 3.2-19,20,23,25, and 27, as

$$U(k_y, k_z) = \int_{-\infty}^{\infty}\int_{-\infty}^{\infty} E(0, y, z)e^{-2\pi i(yk_y+zk_z)}dydz \tag{3.23}$$

$$E(0, y, z) = \int_{-\infty}^{\infty}\int_{-\infty}^{\infty} U(k_y, k_z)e^{2\pi i(yk_y+zk_z)}dk_ydk_z. \tag{3.24}$$

The electric field E is sampled on the plane $x_0 = 0$; note that E and U have different dimensions.

We now consider the associated discrete Fourier transform, on the finite plane of dimension L^2. By analogy to the 1D case (equation 3.20) we define a slightly different vector transform function $A_i(k_y, k_z) = U_i(k_y, k_z)/L^2$ (where $i = x, y, z$ component of each quantity) as the two-dimensional finite Fourier Transform of the 3D complex vector electric field strength $E_i(x_0; y, z)$ (x_0 can be chosen =0).

$$A_i(k_y, k_z) = \frac{1}{L^2}\int_{-L/2}^{L/2}\int_{-L/2}^{L/2} E_i(x_0; y, z)e^{-2\pi i(yk_y+zk_z)}dydz, \tag{3.25}$$

where we note as that in SM97, the numerical scaling prefactor is associated with the negative exponential transform into frequency space. This (finite) integral transform is readily replaced by a discrete summation, where we substitute $y_l = l\Delta$, $z_m = m\Delta$, $k_y = \alpha dk$, $k_z = \beta dk$, and l, m, α, and β are integers, where $\Delta = dy = dz$ is the grid spacing in the cartesian (y, z) DDFIELD grid. From sampling theory, $dk = 1/L$ where L is the full linear extent of the 2D grid of $E(y, z)$ (assumed to be square), and the maximum resolvable spatial frequency is $k_{max} = 1/\Delta$; typically $-k_{max/2} \le (k_y, k_z) \le k_{max}/2$. Then

$$A_i(k_y, k_z) = \frac{1}{(N\Delta)^2}\sum_{-N/2}^{N/2}\sum_{-N/2}^{N/2} E_i(x_0; y_l, z_m)e^{-2\pi i(l\alpha+m\beta)\Delta/N\Delta}\Delta^2 \tag{3.26}$$

$$A_i(k_y, k_z) = \frac{1}{N^2}\sum_{-N/2}^{N/2}\sum_{-N/2}^{N/2} E_i(x_0; y_l, z_m)e^{-2\pi i(l\alpha+m\beta)/N}, \tag{3.27}$$

where here $A_i(k_y, k_z)$ and $E_i(x_0; y_l, z_m)$ have the same units. Using this transform convention, the discrete form of Parseval's theorem reads

$$\sum_{\alpha}\sum_{\beta}|A_i(\alpha, \beta)|^2 = \frac{1}{N^2}\sum_{l}\sum_{m}|E_i(l, m)|^2, \tag{3.28}$$

which is intuitively meaningful because the wave's E field (nominal magnitude E_o) covers all N^2 points in the (y, z) grid, but the equivalent emerging plane wave only occupies a single grid cell in the (k_y, k_z) grid. The convention in Numerical Recipes makes less sense in our context. So, if $|E_o|^2$ is a flux density (energy/area/time/wavelength interval) then so is $|A(\alpha, \beta)|^2$ (leaving aside issues of the permittivity of free space). This relationship was numerically verified in our code.

The orthogonal components E_x, E_y, and E_z are separately transformed and combined. The output A_x, A_y, A_z could be used to calculate polarization state (A_{par}, A_{perp}), which are both, by definition, perpendicular to the ray direction at (k_y, k_z), but because we are only interested in intensity, we simply sum the squares of A_i as noted above.

The discrete transform quantities $A_i(\alpha, \beta)$ represent plane waves with some unpolarized, total flux density $\sum_1^3 |A_i|^2$ propagating in the directions $\theta(k_y, k_z)$, $(\phi - \phi_0)(k_y, k_z)$, where the angles of the emergent rays are defined relative to the normal to the layer and the incident ray direction (θ_0, ϕ_0):

$$k_x = k_o \cos\theta \tag{3.29}$$

$$k_y = k_o \sin\theta \sin(\phi - \phi_0) \tag{3.30}$$

$$k_z = k_o \sin\theta \cos(\phi - \phi_0) \tag{3.31}$$

where $k_o = 1/\lambda$ and we solve at each (k_y, k_z) for $k_x = (k_o^2 - k_y^2 - k_z^2)^{1/2}$. It is thus an implicit assumption here that all propagating waves have wavenumber $k_o = 1/\lambda$; it can be verified numerically that there is no energy at $k > k_o$, as might occur if the the DDFIELD sampling layer at x_o had been placed too close to the scattering layer.

Overly coarse sampling of $k-$space can result in poor estimates of the locations and magnitudes of emergent rays; unfortunately the dimension of the DDFIELD grid is computationally constrained to some degree. We overcome this obstacle by zero-filling the array $E(x_0; y, z)$ out to some considerably larger extent L', retaining the original array as a subset. Upon transforming this larger array we achieve spatial frequency resolution $dk' = 1/L' \ll dk = 1/L$; this high resolution reveals the true locations and amplitudes of the peaks by over-resolving their intrinsic angular width in wavenumber space $dk = 1/L$. Tests conducted using this simple trick provided a very regular and reliable reconstruction in k-space of both the direction and amplitude of incident plane waves crossing the DDFIELD grid in a variety of directions. This is a valuable approach, because the compute time needed to converge a DDFIELD grid of size N^2 is strongly dependent on N, while the time needed to perform an FFT of a significantly zero-filled grid grows only as $N\log N$.

The more highly resolved plane wave fluxes $A_i'(k_y', k_z')$, are smaller in magnitude than a value which lies entirely in a single (k_y, k_z) bin and represents the entire plane wave. This is because, as flux densities, the more highly resolved results of the zero-filled calculation represent the intensity integrated over a smaller solid angle. To obtain the total flux density in the wave, we would sum over the narrow "packet" of rays, each having angular width $dk_y' dk_z'$ lying in a scattered lobe of (larger) angular width $dk_y dk_z$. Nevertheless, an effective *intensity* can be determined for each of these rays, given by its flux divided by its corresponding solid angle. As defined this way, the intensity is invariant to zero-filling, because the flux in a (k_y, k_z) bin simply decreases with the angular width of the bin. That is, $A_i'(k_y', k_z')/dk_y' dk_z' = A_i(k_y, k_z)/dk_y dk_z$. Below, we show how we determine true intensities (flux density per unit solid angle).

From this point on, we assume fluxes are summed over their components i and suppress the subscript i. The next step is converting the angular distribution of plane waves, or flux densities (energy/time/area), $|A(k_y, k_z)|^2$ into intensities (energy/time/area/solid angle). Perhaps the most straightforward approach is to determine the element of solid angle subtended by each grid cell $dk_y dk_z$ at (k_y, k_z): $d\Omega(\theta,\phi) = \sin\theta(k_y, k_z) d\theta(k_y, k_z) d\phi(k_y, k_z)$. Then the intensity is

$$I(\theta,\phi) = |A(k_y, k_z)|^2 / d\Omega(\theta,\phi). \tag{3.32}$$

We have computed the elemental solid angles in two separate ways. One obvious but cumbersome way to calculate $d\Omega(k_y, k_z)$ is to determine the elemental angles subtended by each side of the differential volume element using dot products between the vectors representing the grid points, and multiply them to get the element of solid angle $d\Omega(k_y, k_z)$. Another method makes use of vector geometry to break $d\Omega(k_y, k_z)$ into spherical triangles (Van oosterom and Strackee 1983). These methods agree to within the expected error of the technique. A simpler and more elegant approach is to rewrite equation 3.32 as

$$I(\theta,\phi) = \left(\frac{|A(k_y, k_z)|^2}{dk_y dk_z}\right) \frac{dk_y dk_z}{d\Omega(k_y, k_z)} = \left(\frac{|A(k_y, k_z)|^2}{(1/L)^2}\right) \frac{J d\theta d\phi}{d\Omega(k_y, k_z)}, \tag{3.33}$$

where the Jacobian J relates $dk_y dk_z = J d\theta d\phi$:

$$J = (\partial k_y/\partial\theta)(\partial k_z/\partial\phi) - (\partial k_y/\partial\phi)(\partial k_z/\partial\theta) \tag{3.34}$$

Then from equations (3.32-3.34) above, $J = k_o^2 \sin(\theta)\cos(\theta)$, and

$$I(\theta, \phi) = \frac{|A(k_y, k_z)|^2 (k_o L)^2 \sin(\theta)\cos(\theta) d\theta d\phi}{\sin(\theta) d\theta d\phi} \tag{3.35}$$

$$= |A(k_y, k_z)|^2 \cos(\theta)(k_o L)^2 = |A(k_y, k_z)|^2 \cos(\theta)(L/\lambda)^2. \tag{3.36}$$

This last expression can be thought of physically as the flux coming through an aperture of dimension $L \times L$ (the DDFIELD grid), at a zenith angle θ, distributed into a cone of (diffraction) solid angle $(\lambda/L)^2$. We can also write explicitly $d\Omega = \sin\theta d\theta d\phi = \sin\theta(dk_y dk_z/J) = \sin\theta(1/L^2)/k_o^2 \sin\theta cos\theta = \lambda^2/(L^2\cos\theta)$. Numerical tests confirm that this expression reproduces the directly determined elemental solid angles, so we will use this simpler and more elegant closed-form relationship.

After checking the region of k-space $k_y^2 + k_z^2 > k_o^2$ for nonphysical, anomalous power and thereby validating the location x_0 of the sampled $E(x_0; y, z)$, and converting to intensity, the Cartesian grid of $I(k_y, k_z)$ is splined into a polar grid $I(\mu_i, \phi_j)$ with coordinate values μ_i corresponding to the cosines of the Gauss points in zenith angle from the layer normal. This interpolation is designed to eliminate the nonphysical region $k_y^2 + k_z^2 > k_o^2$ from further consideration and streamline subsequent steps which will use Gaussian quadrature for angular integrations of the intensities.

The radiation on the forward-scattered side of the layer is all-inclusive - that is, includes both the scattered radiation and the radiation which has not interacted with any particles (the so-called "directly transmitted beam"). To extract the directly transmitted beam from the diffusely scattered intensity of interest, we will identify the emergent angle expected to contain the directly transmitted beam ($\mu_0 = \cos\theta_0, \phi - \phi_0$). We will then perform two spline fits: (a) of a small region surrounding the total emergent flux density covering the point ($\mu_0, \phi - \phi_0$), and (b) of the underlying broader, smoother function $T(\tau; \mu_0, \mu, \phi - \phi_0)$ *while ignoring points close to the nominal beam direction* (*ie,* points within the actual angular resolution of the original spatial frequency grid $1/L$). The interpolated value of the underlying smooth function at ($\mu_0, \phi - \phi_0$) will be subtracted from the interpolated value in the emergent direction (obtained from the full flux distribution of (a)) to give the flux density of the directly transmitted beam alone, which will give us the effective layer slant optical depth τ/μ_0 at angle θ_0. For subsequent applications involving the doubling method, it will be assumed that the attenuation of the direct beam through a nonclassical layer of twice the (slant) thickness with the same properties will simply scale as $\exp(-2\tau/\mu_0)$. No such complication afflicts the diffusely reflected radiation.

3.3 Tests

The simplest validity test of our regolith model is simulating a dielectric slab with well known analytical solutions for reflection and transmission given by the Fresnel coefficients. The Fresnel coefficients test the accuracy of the electric field calculated from dipole polarizabilities. The Fourier transform method can be tested by locating the position of the specular beam on the reflected and/or transmitted side of the slab.

3.3.1 Dielectric slab tests

We used the DDA PBC method to simulate a slightly absorbing homogeneous dielectric slab with M=1.5+0.02i. The slab is modeled with 20x2x2 dipoles along its x, y, and z dimensions and is illuminated at $\theta_0 = 40°$. The dimensions of the slab are held constant while the wavelength is varied which results in the characteristic sinusoidal pattern in transmission and reflection as incident radiation sweeps out multiple fractions of the optical path through the layer (see figure 3.4). Figure 3.4 shows the electric field on the transmitted and reflected sides compared with Fresnel's analytical formulae for the same dielectric layer. The agreement is very good, however there is an azimuthal variation of the electric field with respect to the slab which we expected to be uniform for a homogeneous dielectric slab. The variation is smooth and small at less than ten percent level and we will average it out by using many orientations.

To test the FFT method (section 3.2.3) for getting the angular direction of scattered radiation, we analyzed the location of the scattered beam on either side of the layer. We sampled the electric field vector on a 2-D grid of points $N_y = N_z = 64$ where the Fourier transform of the vector field is taken separately for each dimension. The power is obtained by squaring the transformed amplitudes in each dimension. Contour plots (figure 3.5) show the peak of the power spectrum in the reflected region for various incident angles. We can see that as we change the incident radiation angle the emergent intensity changes location in k-space accordingly which confirms that our model is consistent with Snell's law.

Since the PBC calculations are computationally challenging; requiring multiple

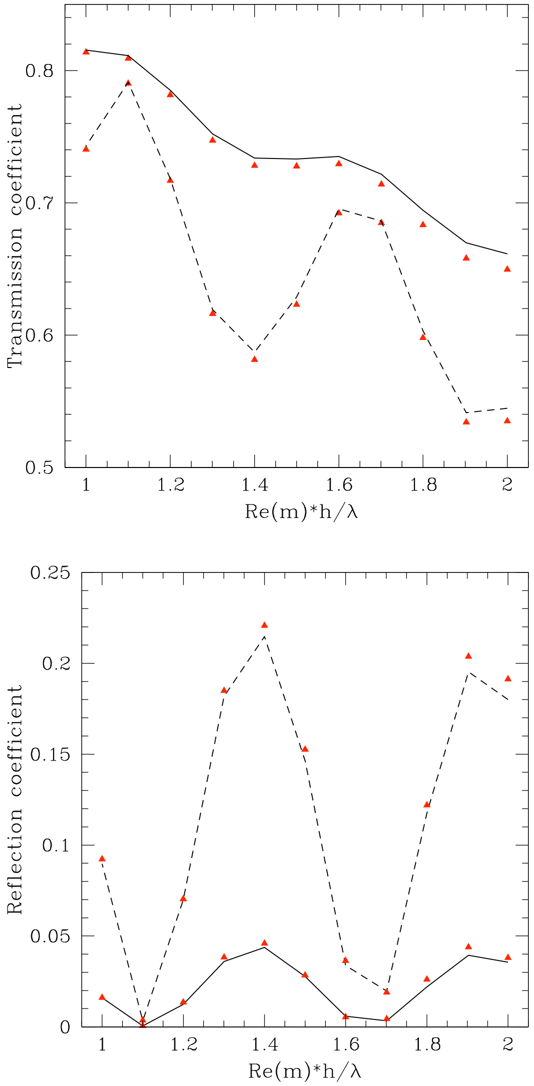

Figure 3.4: (top): Comparison of the transmission coefficient, as a function of wavelength, and for two different planes of polarization TE and TM, for a slightly absorbing dielectric slab as calculated on the TUR by our code (red triangles), and as calculated from Fresnel coefficients for the same slab (solid line for TM and dashed for TE). The slab is h =20 dipoles (6 μm) thick with an index of refraction $m = 1.5+0.02i$, and the wavelength λ varies between 4.5-9μm (see section 3.2). (bottom): Reflection coefficient comparison for the same slab between DDfields calculation and Fresnels analytical expression.

processors and days to reach convergence, it is advantageous to use a more relaxed $|M|kd$ criterion to reduce computation time. So we looked at the variation of the electric field with

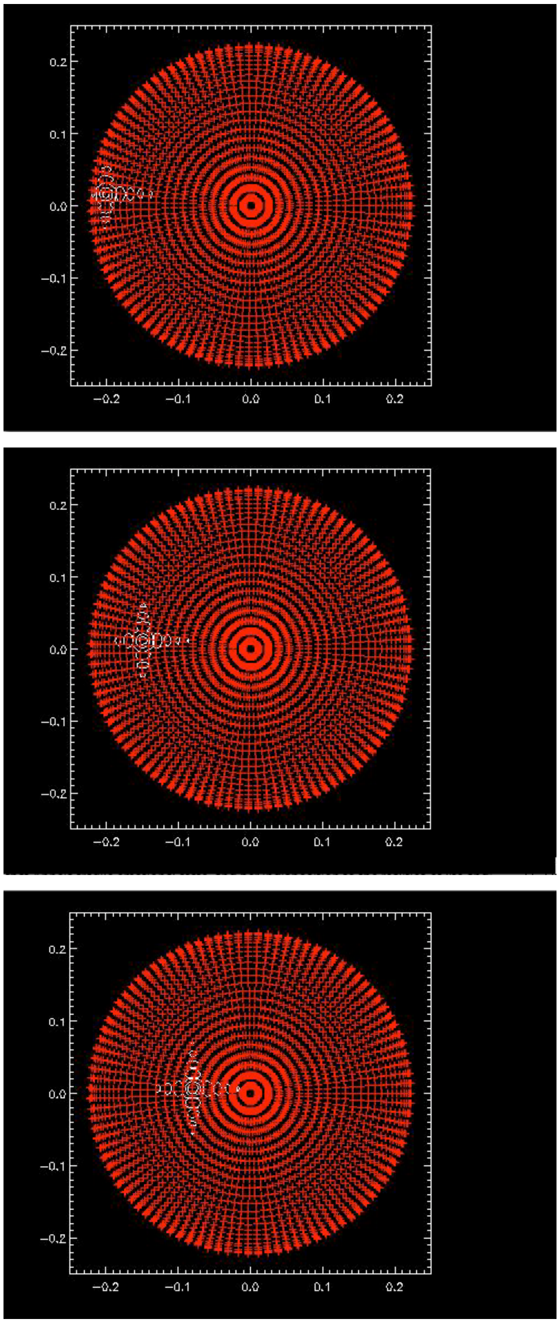

Figure 3.5: (top): Reflected intensity in k-space shown on a polar plot with dimensions (θ, ϕ) for three incident radiation angles: θ_o $=20^\circ$, 40°, and 60° and $\phi_o = 0$ for all cases. The emergent shown as a white circle in the polar plot moves in k-space at the correct emergent angle: $\theta =$ 20°, 40° and 60°.

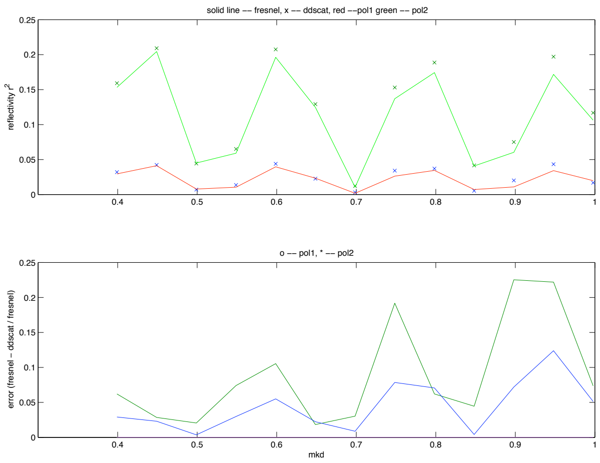

Figure 3.6: Reflectivity from a dielectric layer for various $|M|kd$ values ranging between 0.4-0.9 compared with Fresnel's analytical solution (top). Bottom panel shows the difference between Fresnel's coefficient and the dielectric slab reflectivity divided by Fresnel's value (percent error). The difference between the two starts taking off at $|M|kd = 0.9$.

various mkd values ranging between 0.4-1.0. In figure 3.6 we can see that the field variation and its comparison with Fresnel's coefficients is in good agreement within less than ten percent for $|M|kd$ values below 0.7 and diverges from there. This was a first check to see if we can push the limit on $|M|kd$ and we will further check this for granular layers to make sure we're not introducing large errors in our calculations.

3.3.2 Granular layer

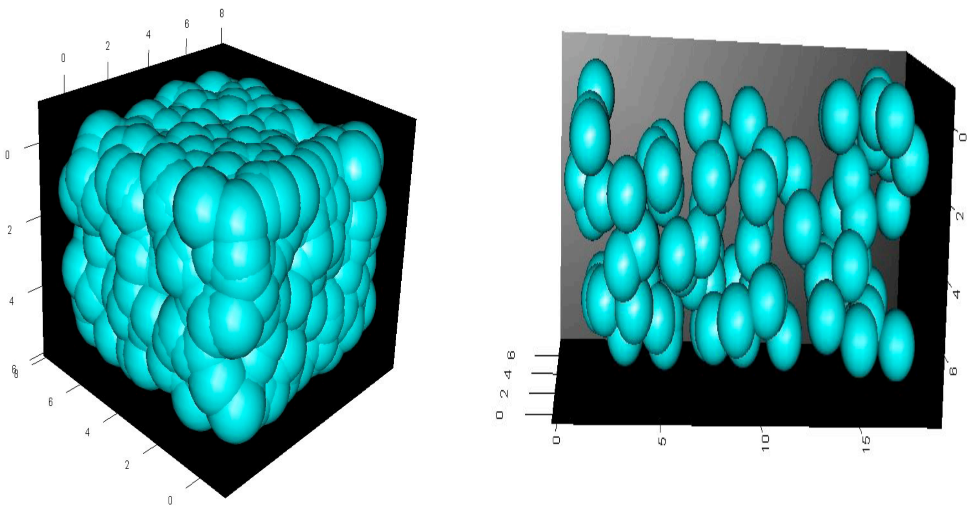

Figure 3.7: (left): Granular TUC constructed by overlapping monomers with %70 packing fraction. (right) Granular TUC with %30 packing fraction.

After gaining confidence that our RRT model can reproduce a dielectric slab we started to model granular layers with diffuse scattered fields. For a first order study we take the simplest approach to generating granular layers by populating the TUC with overlapping spherical monomers of the same size and composition. We use the well known quartz refractive indices for these monomers at 15.5μ wavelength which is a problematic band for current models as shown in figure 3.1. The scattered field from this layer is calculated by DDFIELD for each combination of (incident light polarization, azimuth orientation β with respect to layer normal) separately and averaged incoherently over polarization to get an intensity profile as a function of θ for a given β orientation. The granular TUC's are about five monomers deep and 3-5 monomers across making up a TUC box with 50-100 monomers. The monomers are comparable to the size of the wavelength (complex modeling region of interest) which requires many millions of dipoles to reach adequate accuracy. Due to the large size of these granular TUCs, ddscat takes many iterations to converge on a solution and certain subset of β orientations show large variations in both field measured on the TUR grid, and intensity measured in the angular domain (see figure 3.8). We can see from figure 3.8 that these bad fields and intensities are very distinguishable from the converged solutions and can be thrown out before averaging

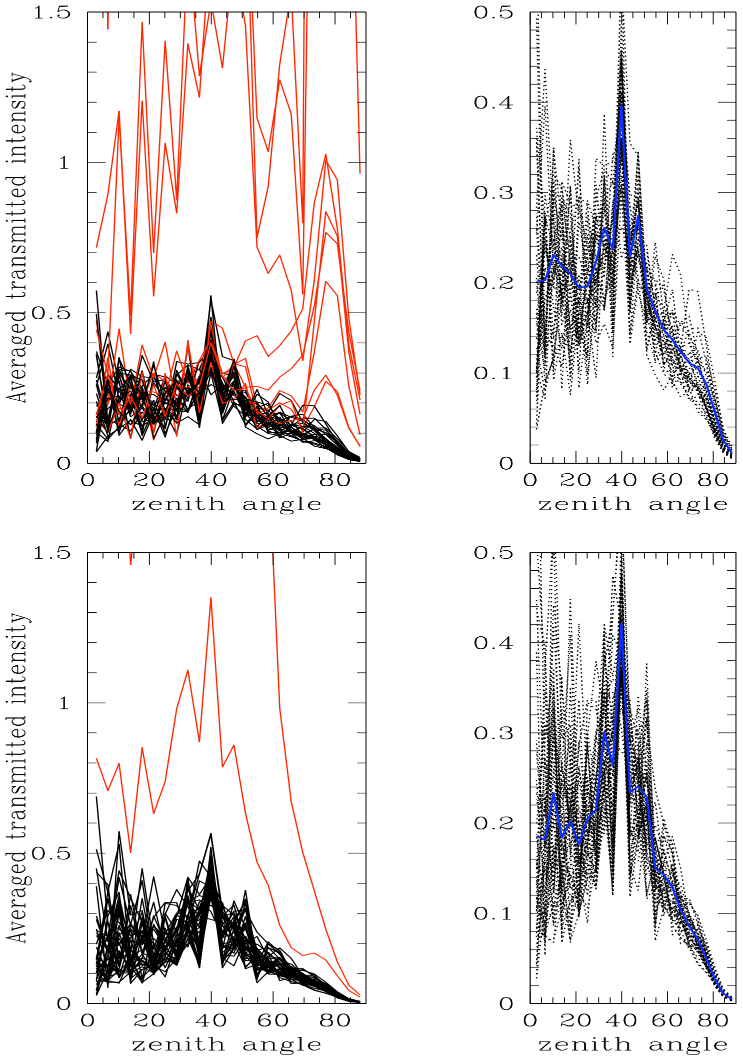

Figure 3.8: Transmitted intensities for various β orientations from a granular layer with $\%70$ filing factor and two mkd criterion (top panels – $|M|kd$=0.5, bottom panels – $|M|kd$=0.8). left panels show abnormal intensities in red and converged intensities in black. We take the average of the converged intensities shown in blue in the right panels. The variation in averaged transmitted intensity is within $\%10$ for the two mkd cases.

over β orientations. There is a similar variation with β in the absorption coefficient Q_{abs} with distinct bad values for non-converged orientations. This is further indication that the abnormally large fields are a result of non-convergence in ddscat rather than a problem with DDFIELD's calculations. Averages over β orientations are again done incoherently and plots of intensities as

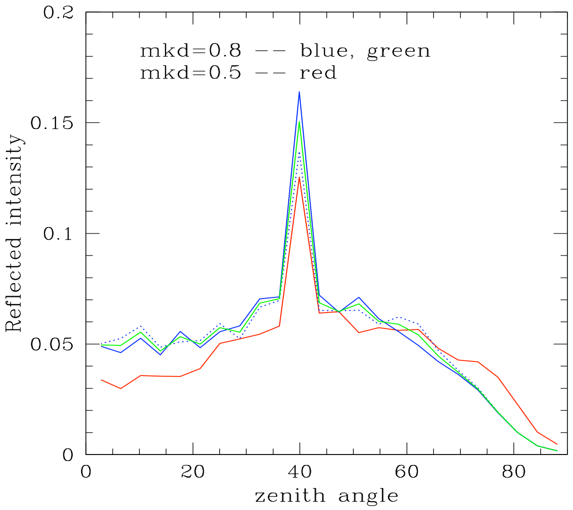

Figure 3.9: Reflected intensities for two realizations (solid and dotted blue, with the average of the two in green) of a granular layer with $\%70$ filling factor and $|M|kd$ = 0.8. The averaged intensity for the same layer with $|M|kd$ = 0.5 is shown in red for comparison. Variations due to granular realizations and larger $|M|kd$ is within an acceptable limit for our initial studies. Its also interesting to note that there is a qualitative difference in the two averaged reflected intensity curves for $|M|kd$ = 0.5 and 0.8. We believe this is due to the change in grain shapes becoming less spherical as the $|M|kd$ criterion is relaxed.

a function of θ (angle from normal) for two cases with different $|M|kd$'s 0.5 and 0.8 are shown in figure 3.9. The field is lumpy as opposed to the dielectric slab's single specular peak due to the granular structure in the layer. There is also a remnant of the 40° specular peak visible in these cases. Its important to note from figure 3.9 that the scattered intensity varies within $\%10$ between the two mkd cases and realizations which means that (1) we don't need to average over too many realizations for an acceptable solution and (2) we can use $|M|kd$ = 0.8 to speed up our runs.

Our final results are granular runs with filling factors varying between $0.1, 0.2, 0.5$, and 0.7. All these layers are modeled with the same amount of quartz material but varying TUC volume to simulate various porosities. This way the material density of the layers is the same and we can isolate the effect of close packing on the scattered intensity. We calculate filling factors for these layers by taking the ratio of the number of quartz dipoles to vacuum dipoles in the TUC box. The results are shown in figure 3.10 where the most porous layers are more reflective and the dense layer is packed to the point where it resembles a

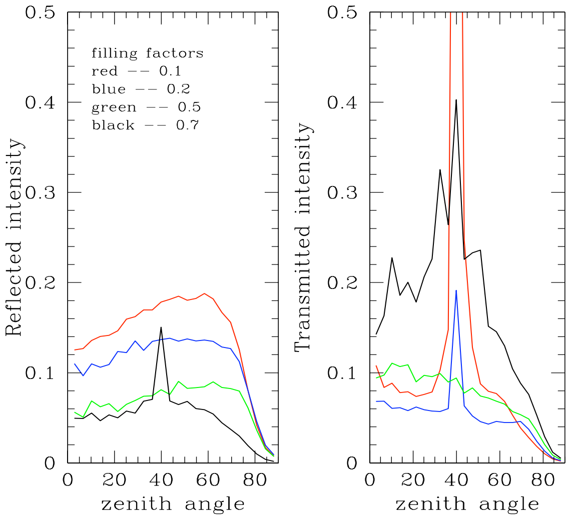

Figure 3.10: Reflected and transmitted intensity as a function of zenith angle for granular layers of various filling factors. All layers are composed of quartz monomers and incident upon by a 15.5μ beam at 40° zenith angle. The densely packed layer in black is resembling a homogeneous layer with a specularly reflected and directly transmitted peak present at 40°. The less dense layers are more reflective and less transmissive. There is a transition layer at $\%50$ filling factor which has no directly transmitted beam (where interface terms causing phase shift of light as it travels between material and vacuum play an important role in transmission).

homogeneous dielectric layer with a rough surface. An electromagnetic beam traveling through a homogeneous dielectric layer is attenuated with an optical depth τ given by the extinction coefficient of the material $4\pi n_i/\lambda$ where n_i is the imaginary refractive index. In contrast for the highly porous layers where there are large vacuum gaps between monomers, the optical depth $\tau = Q_{ext} * n\pi r^2$ where Q_{ext} is the extinction coefficient and r is the radius of each monomer. n is a particle density defined as the number of particles per surface area of the layer. The $\%50$ filling factor is an interesting transition region where the monomers are closely packed enough to introduce interference effects and the vacuum gaps are large and abundant enough to contribute to interface terms as discussed in chapter 2. The interface terms are so significant that they cancel the directly transmitted beam through this layer.

3.4 Conclusion

I have developed an end-to-end approach for regolith radiative transfer for monomers Of arbitrary size, shape, and packing density. The various parts of this approach have been thoroughly tested. PBC was tested by generating a dielectric layer with its transmission and reflection coefficients compared to Fresnel's analytical coefficients with good agreement. The FFT method for localizing the beam in k-space was tested by moving the zenith angle of the incident beam which resulted in the scattered beam emerging at the correct emergent angle in accordance with Snell's law.

There are intriguing results from the granular layers where its apparent in three different layer porosities that extinction does not scale simply as τ of independent particles, and spacing does matter.

3.4.1 Acknowledgements

We are very grateful to Essam Marouf for insightful discussions and help leading us to the right track with the design of our model. Also, we'd like to thank Terry Nelson, and especially Art Lazanoff for help getting the optimizing done, Denis Richard for trouble shooting and running the code, and Bob Hogan for automating the various parts of the model. The research was partially supported by the Cassini project and partially by a grant to JNC from NASA's Planetary Geology and Geophysics program.

3.5 References

Conel, J. E. (1969) J. Geophysical Research, 74, 1614-1634

Cuzzi, J. N. and Estrada, P. E. (1998) Icarus, 132, 1-35

Cuzzi, J. N., J. J. Lissauer, L. W. Esposito, J. B. Holberg, E. A. Marouf, G. L. Tyler, A. Boischot (1984). In Planetary Rings. Eds. R. Greenberg and A. Brahic. U. Arizona Press. Tucson, Arizona.

Draine, B. T. and Flatau, P. J. (1994) J. Opt. Soc. Am. 11, 1491-1499

Esposito, L.W., J.N. Cuzzi, J.B. Holberg, E.A. Marouf, G.L. Tyler, and C.C. Porco 1984. In Saturn. Eds. T. Gehrels and M Mathews. U. Arizona Press. Tucson, Arizona.

Goody, R. M. (1964) Icarus, 3, 98-102

Hansen, J. E. (1969) Astrophys. J. 155, 565

Hansen, J. E. and Travis, L. D. (1974) Space Science Reviews 16, 527-610

Hapke, B. (1981) J. Geophys. Res., 86, 4571-4586

Hapke, B. (1999) J. Quant. Spectrosc. Rad. Transf. 61, 565-581

Mandel, L. and Wolf, E., (1994) Optical Coherence and quantum optics (New York: Cambridge University Press)

Moersch, J. E. and Christensen, P. R. (1995) J. Geophysical Research, 100, 7465-7477

Mustard, J. F. and Hays, J. E. (1997) Icarus, 125, 145-163

Plass, G.N., G.W. Kattawar, and F.E. Cathcings 1973. Appl. Opt., vol. 12, pp 314-329.

Pollack, J. B. and Cuzzi, J. N. (1979) J. Atmospheric Sciences, 37, 868-881

Poulet, F., D. Cruikshank, J. N. Cuzzi, and T. Roush (2003) Astronomy and Astrophysics 412, 305-316

Poulet, F., J. N. Cuzzi, D. Cruikshank, T. Roush, and C. Dalle Ore (2002a) Icarus, 160, 313-324

Press, W. H., S. A. Teukolsky, W. T. Vetterling, and B. P. Flannery, (1999) Numerical recipes in FORTRAN 77: the Art of Scientific computing (New York: Cambridge University Press)

Purcell, E. M., and C. Pennypacker (1973) Astrophys. J. 186, 705-714

Shepard, M. and P. Helfenstein (2007) Journal of Geophysical Research, Volume 112, Issue E3, CiteID E03001

Shkuratov, Y. G., M. A. Kreslavsky, A. A. Ovcharenko, D. G. Stankevitch, and E. S. Zubko (1999a) Icarus 141, 132-155

Shkuratov, Y. G., Y. Starukhina, H. Hoffmann, and G. Arnold (1999b) Icarus 137, 235-246

Spilker, L. J., S. H. Pilorz, B. D. Wallis, S. M. Brooks, S. G. Edgington, F. M. Flasar, J. C. Pearl, M. R. Showalter, C. Ferrari, R. K. Achterberg, C. A. Nixon, P. A. Romani, and the Cassini CIRS Team (2005) 36th LPSC, League City, Texas, abstract no. 1912

Stoica, P. and Moses R. L., (1997) Introduction to Spectral Analysis (New Jersey: Prentice Hall)

Van oosterom, A., and Strackee J. (1983) IEEE, BME-30 125-126

Wiscombe, W.J., 1975a. J. Quant. Spectrosc. Radiative Transfer, vol 16, pp. 477-489.

Wiscombe, W.J., 1975b. J. Quant. Spectrosc. Radiative Transfer, vol 16, pp. 637-658.